2009

Optical detection of CO and H2 based on surface plasmon resonance with Ag-YSZ, Au and Ag-Cu nanoparticle films

Denis Kitenge
University of South Florida

Optical Detection of CO and H_2 Based on Surface Plasmon Resonance with Ag-YSZ, Au and Ag-Cu Nanoparticle Films

by

Denis Kitenge

A thesis submitted in partial fulfillment
of the requirements for the degree of
Master of Science in Mechanical Engineering
Department of Mechanical Engineering
College of Engineering
University of South Florida

Major Professor: Ashok Kumar, Ph.D.
Frank Pyrtle III, Ph.D.
Muhammad Rahman, Ph.D.

Date of Approval:
November 4, 2009

Keywords: gas sensors, pulsed laser deposition, thin film, absorption, critical angle

I would like to dedicate this thesis to:
my late mother, Ema Marie-Rosalie, for teaching me how to love the Lord,
and to my late father, Daniel Longanga, for teaching me that working hard is the ingredient for success.

ACKNOWLEDGEMENTS

I would like to express my deep gratitude to Dr. Ashok Kumar, my major advisor, and committee members, Dr. Muhammad Rahman and Dr. Frank Pyrtle III, for their valuable insights and suggestions. I am grateful to Mr. Bernard Batson (Director, Diversity and Outreach Programs Director who has provided financial support from different grants. I am also thankful to Dr. Rakesh Joshi who provided help and encouragement during this work. A special thanks to all my friends who stand by me in challenging moments of my life, for their help and support throughout this endeavor. The work was supported by NSF through NIRT # ECS 0404137, Graduate Research Supplement Program, and NSF-FGLSAMP Bridge to Doctorate Program.

TABLE OF CONTENTS

LIST OF TABLES

LIST OF FIGURES

OPTICAL DETECTION OF CO AND H_2 BASED ON SURFACE PLASMON RESONANCE WITH Ag-YSZ, Au AND Ag-Cu NANOPARTICLE FILMS

Denis Kitenge

ABSTRACT

Silver, gold, and copper metallic nanoparticle films have been utilized in various MEMS devices due to not only their electrical but also their optical properties. The focus of this research is to study the detection at room temperature of carbon monoxide (CO) and hydrogen (H_2) via Surface Plasmon Resonance (SPR) phenomenon of silver-embedded Yttrium Stabilized Zirconium (Ag-YSZ) nanocomposite film, gold (Au) nanoparticle film, and an alloy film of silver-copper (Ag-Cu) , grown by the Pulsed Laser Deposition (PLD).

To determine the appropriate film materials for quick and accurate CO and H_2 detection at room temperature with the PLD technique, the growth process was done repeatedly. Optical tools such as X-Ray Diffraction, Alpha Step 200 Profilometer, Atomic Force Microscopy, and Scanning Electron Microscopy were used to characterize thin films. The gas sensing performance was studied by monitoring the SPR band peak behavior via UV/vis spectrophotometer when the films were exposed to CO and H_2 and estimating the percent change in wavelength. The metallic nanoparticle films were tested for concentration of CO (100 to 1000 ppm) and H_2 (1 to 10%). Silver based sensors were

tested for the cross-selectivity of the gases. Overall the sensors have a detection limit of 100 ppm for CO and show a noticeable signal for H_2 in the concentration range as low as 1%. The metallic films show stable sensing over a one-hour period at room temperature. The SPR change by UV/vis spectrophotometer shows a significant shift of 623 nm wavelength between 100 ppm CO gas and dry air at room temperature for the alloy films of Ag-Cu with a wider curve as compared to silver and gold films upon their exposure to CO and H_2 indicating an improvement in accuracy and quick response.

The results indicate that in research of CO and H_2 detection at room temperature, optical gas sensors rather than metal oxide sensors are believed to be effective due to not only the absence of chemical involvement in the process but also the sensitivity improvement and accuracy, much needed characteristics of sensors when dealing with such hazardous gases.

CHAPTER 1: INTRODUCTION

1.1 Background

Health and safety issues associated with environmental pollutants and hazardous gases such as CO, H_2 , HS, CO_2, NO_x and NH_3 have always been the subject of priority in materials research. With the rising desire for better manufacturing of goods and the increasing concern about air quality due to pollution, it has become an obligation to develop not only highly sensitive but accurate gas sensors to cut down the number of accidents and the loss of lives, and environmental hazards, due to gas leakages [1]. The main purpose of having such sensors should be the setting of a clear and distinct alert announcing the presence of a gas in a location. Metal oxide sensors have been a significant part of the gas sensor technology and remain a widely used choice for a range of gas species [2]-[6]. The working principle of a typical resistive metal oxide gas sensor is based on a shift of state of equilibrium of the surface oxygen reaction due to the presence of a target analyte. The change in concentration of chemisorbed oxygen is recorded as a change in resistance of the gas-sensing material.

Optical gas sensors based on surface plasmon resonance are useful type of gas sensors used along with metal oxide sensors for detection of toxic gases in the past. The sensing mechanism based on SPR spectroscopy is related to the measurement of a small

change in refractive index that occurs in response to an analyte binding at or near the surface of a noble metal such as Au and Ag [7].

Surface Plasmon Resonance was first observed by Wood [8] to describe narrow dark bands in the spectrum of the diffracted light when a metallic diffraction grating with polychromatic light. These bands are associated with the excitation of electromagnetic surface waves on the surface of the diffraction grating. More recently, the phenomenon has been studied and applied in bio-sensing field, biopharmaceutical manufacturing, the spacecraft industry, sound-recording technology, and windows surface coating [9]-[10]. The main advantages of SPR technology include high sensitivity, label-free, real-time and rapid detection [11]. This rapid detection is due to the fact that SPR of metal-dielectric composite films formed by using metal nanoparticles embedded in a dielectric is very sensitive to the changes in the refractive index induced by physical absorption or chemical reactions on the surface of the material [12]-[15].

1.2 Surface Plasmon Resonance (SPR)

Surface Plasmon Resonance is described as the quanta of waves generated by collective effects of a considerable number of electrons in matter. Metals show plasmon effect because they have high density of free electrons. Recently, surface plasmons resonance has become a promising technique of understanding various relationships between molecules. Plasmon sensitivity depends mostly on particle size and shape, refractive index of the medium and the dielectric constants of the metal.

For most metals the plasmon energy is correlated to ultraviolet photon energy. For silver and gold the plasmon energy is as low as that of visible photon making it possible to be excited with a light such as laser light. Figure 1.1 shows the visible spectrum where silver and gold plasmon energy is located.

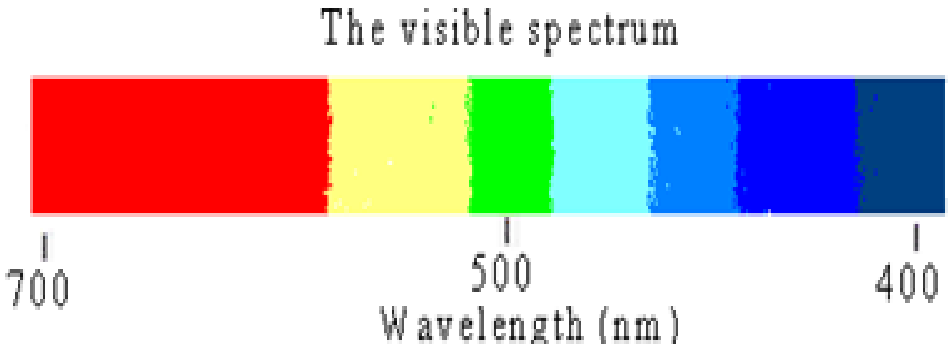

Figure 1.1 Visible range of electromagnetic radiation

These specific plasmons exist at the surface and they have been utilized for many applications. Plasmons are also known as charge-density oscillation of free electron density against the fixed positive ions occurring at the interface of two media with dielectric constants of opposite signs. Normally associated with charge density is an electromagnetic wave or the field vectors which reach their maxima at the interface and decay evanescently into both media [16]. The propagation of wave plasma is done in the direction parallel to the metal surface. Given the free space wave number (k), the dielectric constant of the metal (ε_m) and the refractive index of the dielectric (n^2_s), the propagation constant of the surface plasma wave (β) is calculated following this equation:

$$\beta = k\sqrt{\frac{\varepsilon_m n_s^2}{\varepsilon_m + n_s^2}} \qquad (E^{qn}.\ 1)$$

The dielectric constant refers to a number relating the ability of a material to carry alternating current to that ability of a vacuum [17]-[19]; for a particular material or medium and wavelength, refractive index is the ratio of the velocity of light in a vacuum to that in the material or medium [20]. Table 1.1 gives the dielectric constants and refractive indices of materials of interest for this work [21]-[22].

Table 1.1 Dielectric constants and refractive indices of materials of interest

Material	Dielectric Constant	Refractive Index
Silver	complex number	1.35
Copper	complex number	2.43
Gold	complex number	0.47
Hydrogen	1.000284 at 100° C	1.000132
Carbon monoxide (CO)	1.00070 at 23° C	1.000340
Air (dry)	1. 000536 at 20° C	1.0002926

In this study, the absorption band exhibited as SPR arises at the resonance of the incident photon frequency with collective oscillation of the conduction electrons in the metal surfaces. This phenomenon is known as the Localized Surface Plasmon Resonance (LSPR) [23]-[24].

1.3 Parameters of Surface Plasmon Resonance Based Sensors

1.3.1 Sensitivity

An optical sensor is a device which converts the quantity being measured (measurand) to another quantity (output). This is typically encoded into one of the characteristics of a light wave. Figure 1.2 diagrams the main components of a SPR sensor aligned in a sequential order of a normal operation

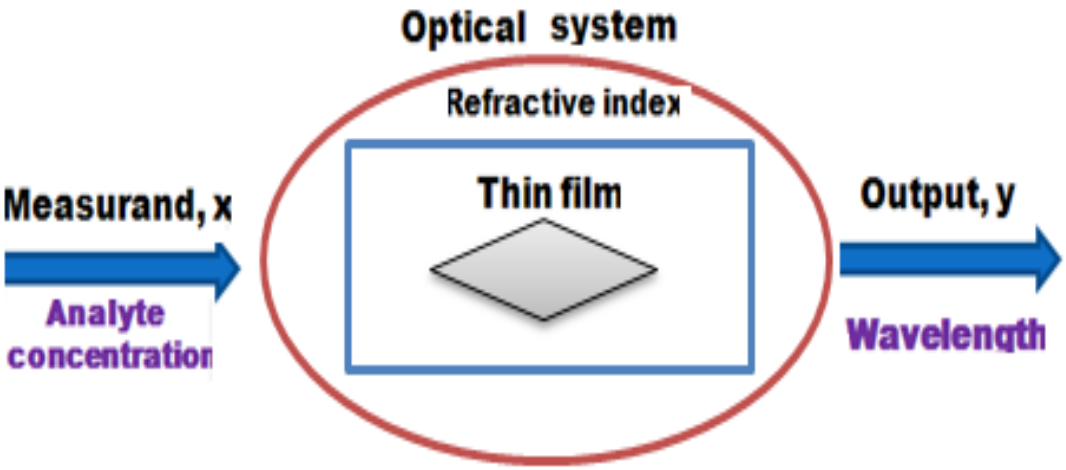

Figure 1.2 Schematic diagram of SPR sensor

The measurand is followed by the optical system housing the thin film, then by the output quantified as wavelength. SPR sensor sensitivity is essentially its ability to respond to an analyte. To a concentration of analyte *c* the sensitivity of an SPR sensor can be written as [25]:

$$S_c = \frac{\partial Y}{\partial c} \qquad (\text{E}^{\text{qn}}.\ 2)$$

In the present study, sensor sensitivity is referred to as the change of SPR band peak which mainly depends on the refractive index of the medium, size and shape of particles, and the nature of the surface material. SPR sensor sensitivity measurement is estimated as a percent change for SPR peaks following this expression:

$$\left(\frac{\lambda_{gas} - \lambda_{no\,gas}}{\lambda_{no\,gas}}\right)(100)$$

Technically the SPR sensor sensitivity in our study has two contributors: the wavelength obtained when the film is exposed to dry air and the wavelength when the targeted gas is present.

1.3.2 Resolution

Typically a sensor is a device that involves change and response. However, determining how much change is needed to create a response is the real issue in sensing technology. Resolution of the SPR sensors defines the smallest change in the bulk refractive index that produces a detectable change in the sensor output [26]. Such change is measured and determined.

There are times when changes are introduced into the sensing device without being desired. The intensity of light, for example, can cause fluctuation and lead to unwanted responses. To avoid fluctuation a stable light source is needed to improve sensor reliability. In sensor resolution is the limit of detection. In this study, the expression limit of detection is adopted when CO and H_2 are monitored via the SPR band shifts.

1.3.3 Selectivity or Cross-reactivity

In the normal conditions a gas sensor detects the presence of a particular gas. However, it is very important to evaluate the ability of a sensor to respond to a specific gas exposure while another gas is present at a low concentration. In this study we introduce H_2 while exposing the sensing silver film at the exposure of CO to determine the cross selectivity. The following expression was used to do the calculations:

$$\left(\frac{\lambda_{H_2} - \lambda_{CO}}{\lambda_{H_2}}\right)(100)$$

1.4 Surface Plasmon Resonance Materials: Silver, Copper and Gold

Silver (Ag), copper (Cu) and gold (Au) shows the characteristics of surface plasmon resonance. All three have one electron in the outer atomic shell. Those materials have ability to exhibit surface plasmon resonance absorption bands in visible light [27]. These bands undergo some change in the vicinity of gas flow therefore; become a reliable indicator when used as a mode of assessing gas concentration in an

environment. Silver, Gold and Copper have one single electron (e^-) occupying the last energy level. This conduction electron is the driving force for generating a plasmon. The bands produced by silver nanocrystals are not always stable at high temperatures due to oxidation [28]-[29]. To prevent the Ag film from oxidation we have chosen (YSZ) as the host material [30], which is chemically and mechanically stable [31].

CHAPTER 2: EXPERIMENTAL METHOD

2.1 Pulsed Laser Deposition (PLD)

Pulsed Laser Deposition (PLD) was used to grow the thin films for sensing applications. This deposition procedure allows a laser pulse to enter through a window into a vacuum chamber and impinges on the material to be deposited [32]. Laser pulse (width 20 – 30 nanosecond) is focused to an energy density (~1 – 10 J/cm^2) to vaporize a few hundred angstroms of surface material (called the "plume") in the form of neutral or ionic atoms and molecules with electron-volt kinetic energies which then deposit onto the substrate positioned in front of the target [33]. The distance between the target and the substrate can be adjusted based on the target structure and the type of the film to be fabricated. Excimer laser at lower power densities have been used to deposit semiconducting and superconducting thin film from bulk targets. Prior to the deposition the vacuum chamber needs to be evacuated from the atmosphere by using a roughing pump to 30 m Torr. The Turbo molecular pump can be activated if a high vacuum is needed. PLD parameters for thin film fabrication have been found to be different from other deposition methods. Pulse laser radiation is used for material vaporization and the deposition of thin film. Figure 2.1 is a schematic diagram of a PLD vacuum chamber, while Figure 2.2 displays the entire PLD system.

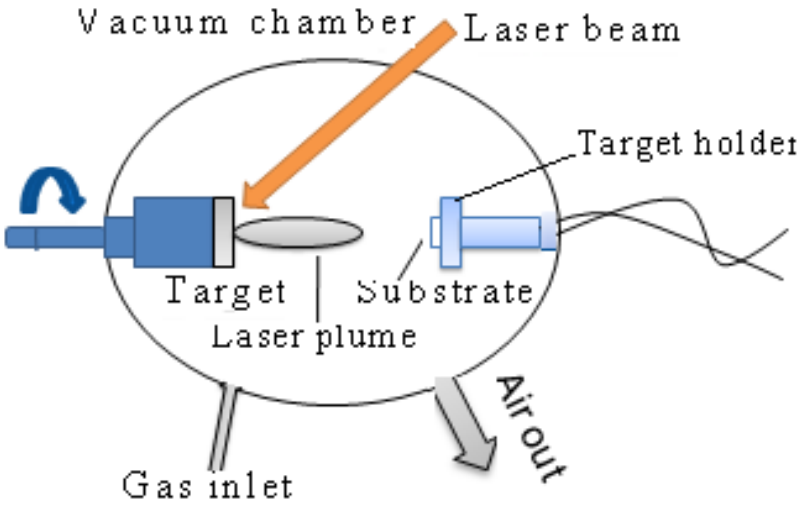

Figure 2.1 Schematic diagram of a PLD vacuum chamber

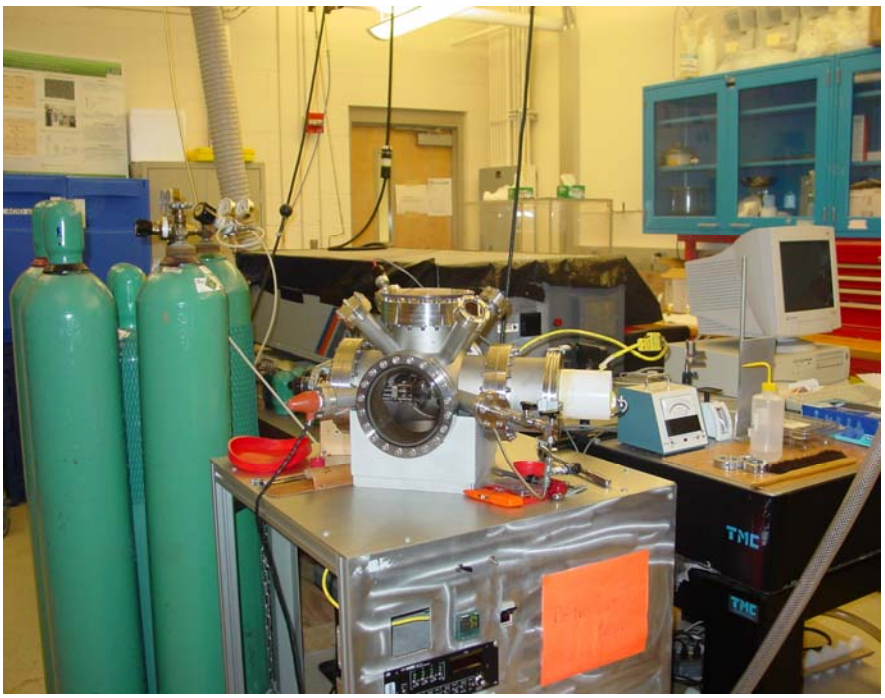

Figure 2.2 PLD vacuum chamber and apparatus at USF

During this procedure the laser radiation is absorbed by a solid surface and the electromagnetic energy is converted into electronic excitation and then into thermal to cause evaporation, ablation, excitation, plasma formation, and exfoliation [42]. Figure 2.3 shows plasma generated during a deposition by PLD of YSZ at 400° C.

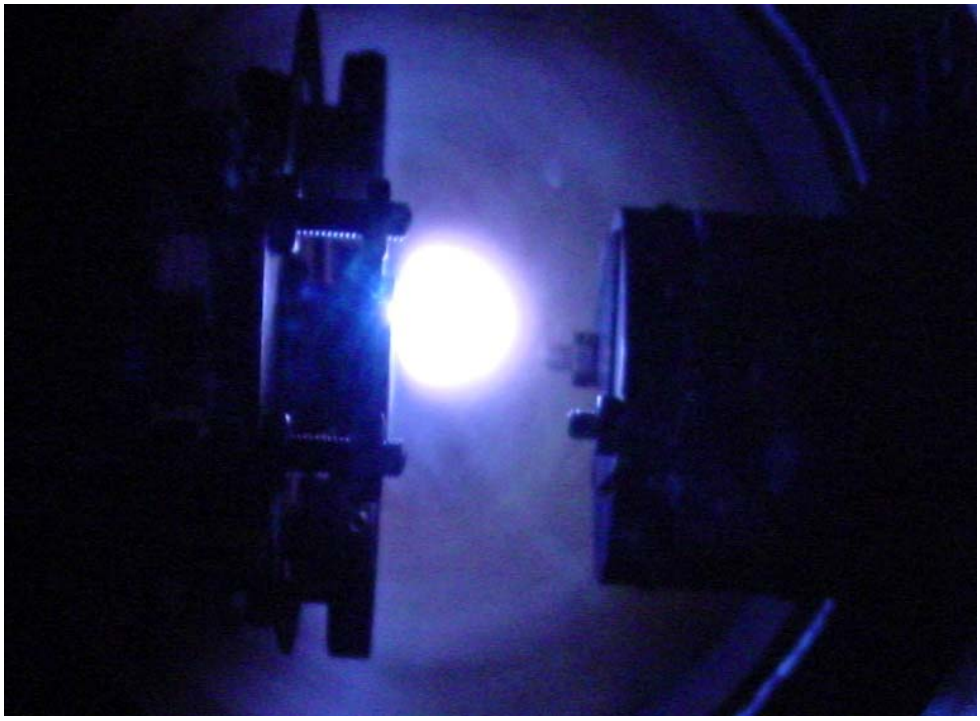

Figure 2.3 Plasma emissions in the vacuum chamber

Besides its simplicity and versatility, PLD offers other advantages that make it a phenomenal deposition technique such as its ability to preserve the stochiometry of a multicomponent system. PLD is proven to be the appropriate technique for thin film fabrication needed for this study.

2.1.1 Optimization of Parameters for PLD

2.1.1.1 Target-to-Substrate Distance

Target to substrate distance is a critical parameters for growth of films. Substrate should have an optimized distance from the target holder to receive the ejected ions from the target. The maximum possible distance between target holder assembly and the substrate is 90 cm. Substrate to target distance is useful to control the grain size of the particles in the films. Higher the distance lowers the particle size.

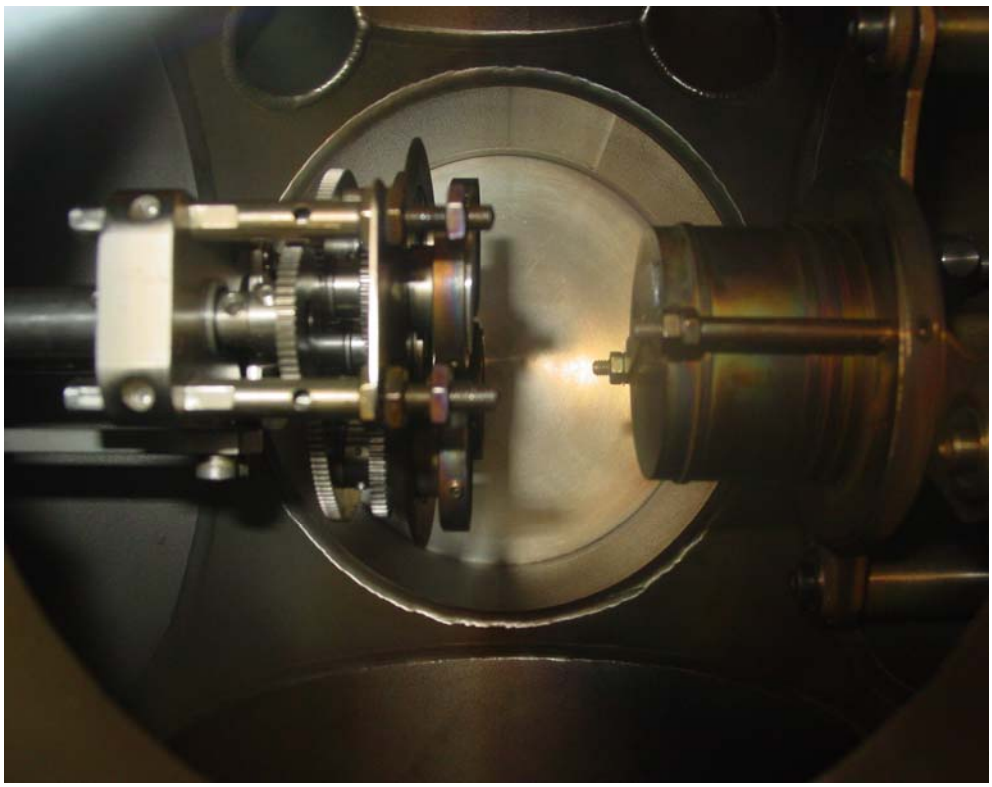

Figure 2.4 Target-to-substrate distance inside PLD vacuum chamber

Figure 2.5 Substrate holder assembly

2.1.1.2 Effect of Temperature on Films Properties

Optimized Temperature is important in order to grow the film with required properties. Most films used in this study were grown at 23° C (room temperature). However the effect of temperature on morphology of the films was studied and will be discussed in next chapter. In the PLD used for this study a thermo couple is built into the system to record the inside vacuum temperature and display it in a small window as shown in Figure 2.6

Figure 2.6 Temperature displayed inside the vacuum chamber

2.2 Microstructure (X-Ray Diffraction)

In this study crystallographic structure of silver, copper and gold was characterized using X-Ray Diffraction. A typical XRD is a technique utilized to determine grain size and preferred orientation in polychrystalline or powdered solid samples. Due to the fact that the wave lengths used in X-rays are very small they can penetrate a considerable number of planes in the crystal, and therefore give information about crystal orientation, material crystallite thickness, the distance between planes lying in atoms, and even residual stress in the film. The spacing between atoms is determine by the use of Bragg's equation given in Figure 2.7 where

n = integer representing the order of peak diffraction

λ = wavelength of x-Ray

d = inter-planar distance

Θ = scattering angle

'*ACB*' = $n\lambda$

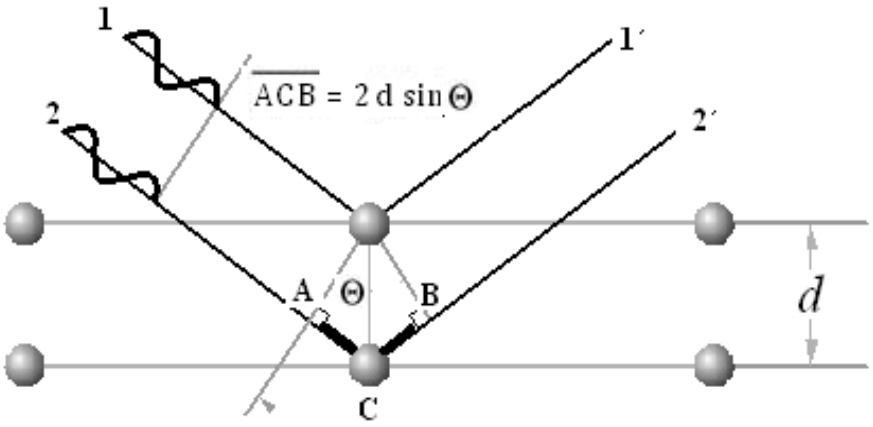

Figure 2.7 Bragg's law

Average grain size can be calculated using the Scherrer's equation given as:

$$t = \frac{k\lambda}{B\cos\theta_B} \qquad (E^{qn}.\ 4)$$

Diffracted X-rays from thin film samples pass through the soller slit, which limits divergence of X-rays in vertical direction. After getting diffracted by a diffracted beam monochromator (graphite plate crystal), the signal is fed to a photomultiplier tube (PMT) interfaced to a personal computer which stores intensity vs. 2θ data in a file. 2θ values for the peaks were used to determine the crystal structure and lattice parameter (s) of the film materials with the help of the Bragg's equation.

2.3 Atomic Force Microscopy (AFM)

Surface morphology of Ag, Cu, Au and YSZ were studied using AFM (Atomic Force Microscope). AFM is a technique used to analyze the surface of materials with magnifications up to 10^8. AFM provides three-dimensional images from conducting or non-conducting samples with extraordinary topographic contrast, direct height measurement and unobscured view of surface features without any sample preparation. Figure 2.6 below shows an atomically a sharp tip made of silicon extended down from the end of a cantilever with feedback mechanisms that enable the piezo-electric scanners to maintain the tip at a constant force or height above the sample surface.

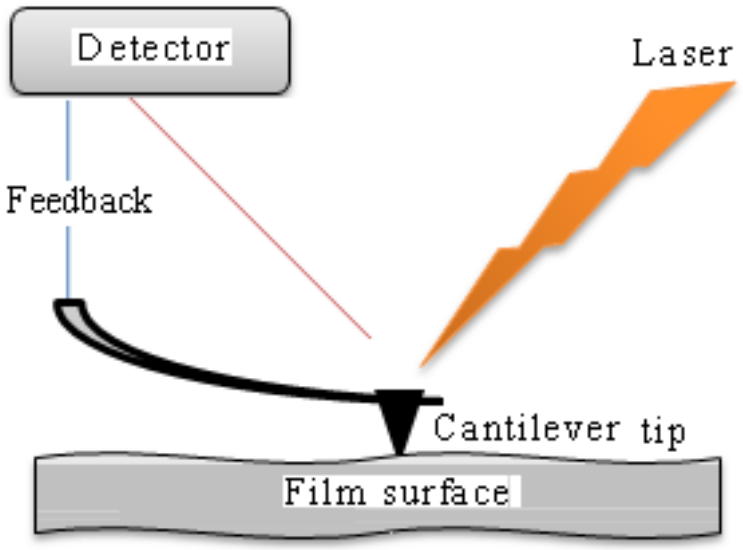

Figure 2.8 Atomic force microscope block diagram

AFM relies on the interatomic van der Waals forces as the factor creating the interaction mechanism between the tip and the sample. Deflection is being done by a laser beam making the system substantially more effective. AFM operates in three modes namely, the contact mode, the non contact mode and the tapping mode. In the contact or repulsive mode, the AFM tip makes contact with the sample, the sample and tip interact by repulsive forces due to quantum mechanical exclusion principle. This mode provides the best resolution but the tip can deform the surface of the sample due to excessive cantilever force on tip against the sample. In the non-contact mode however the AFM cantilever is vibrated within tens to hundreds of Angstroms of the specimen surface; the van der Waals, magnetic or capillary forces produce images of topography with lower poor resolutions than from the contact mode. In the tapping mode (intermittent- contact mode) the vibrating cantilever tip is brought closer to the sample so that, at the bottom of its traverse, it just barely hits the sample resulting in smaller damage to the sample than in the contact mode.

2.4. Scanning Electron Microscopy (SEM)

In the operation of SEM (Hitachi S-800, figure 2.7) a tungsten tip launches a high-energy beam of electrons in a raster scan pattern in vacuum conditions to avoid any possible interference between the beam and the atmosphere. As electrons interact with the atoms that make up the sample, secondary back-scattered electrons from the sample are generated and signals are produced, revealing the arrangement of different elements in the sample, containing information about the sample's surface topography,

composition and electrical conductivity. In this work SEM was used to reveal the size of particles as they play a crucial role in sensing mechanism. The range of magnification for the SEM is up to 300,000 times of the actual size. In addition, its electron beam is used to perform chemical analysis on microstructures below 1 micron in size using an X-ray spectrometer.

Figure 2.9 Hitachi S-800

2.2.5 UV/vis Spectrophotometer

UV/vis spectrophotometer in absorption mode was used to measure SPR peak behavior of silver, gold and silver-copper films. Essentially, the UV/vis spectrophotometer allows interaction between the film, a liquid solution or a solid material and a monochromatic light to take place in a cell isolated from the outside light. As result, the variables such as transmittance, reflectance, and absorbance are obtained [34]. The main components of the equipment are: a source generating a broad band of electromagnetic radiation, a dispersion device selecting a particular wavelength, a chopper dividing the paths of light and a detector measuring the intensity of radiation. Figure 2.10 shows UV/vis spectrophotometer with the optical system displaying the optical system open and the sample area magnified to the right.

Figure 2.10 UV/vis spectrophotometer with optical system open

The working principle of a typical spectrophotometer is based on the use of light that becomes monochromatic passing through a dispersion device and is launched onto the chopper, which switches the light path between a reference optical path and the sample optical path to the detector. The chopper rotates at such speed that alternate measurements of blank and sample occur several times per second. The degree of interaction of the sample with radiation (transmittance or absorption) is determined by measuring both the intensity of the incident radiation or I_0 (without the sample) and the transmitted intensity or I (with the sample). In this respect, Transmittance (T) and Absorbance (A) are defined as follows:

$$T = \frac{I}{I_o} \quad \text{or} \quad \%T = \frac{I}{I_o}(100)$$

$$A = - \log T$$

The UV/vis spectrophotometer was not designed to test the gas concentration therefore, an additional component was designed and assembled to accommodate the film setting and gas flow for measurement of SPR band behavior. The gas-sensor cell testing assembly is a 4 x 4 x 2 cm, 606 aluminum box with the main opposite sides covered with Plexiglas making a path to laser light as shown in figure. The inlet and outlet gas tubing and the fittings are made of stainless steel. In order to avoid gas leak a teflon is used in the fittings. Once integrated in the optical unit, the film holder is designed to remain

steady, to avoid any unnecessary movement that would introduce random error in the measurement. Figure 2.16 displays the cell assembly and its main parts.

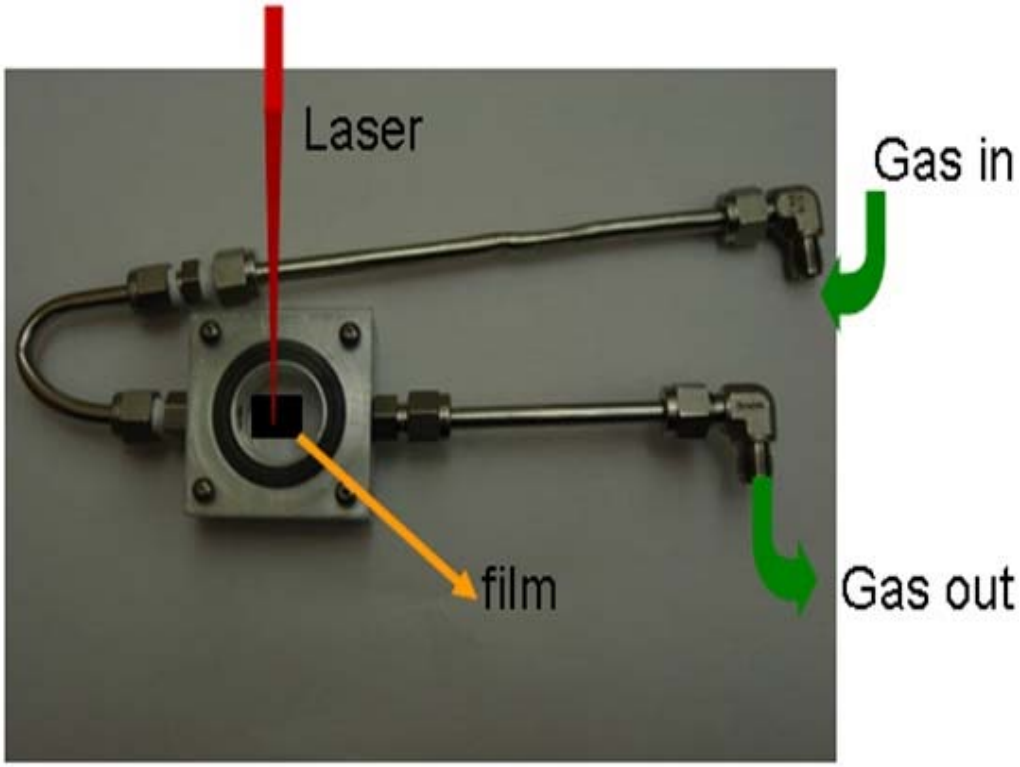

Figure 2.11 Gas-sensor cell testing assembly

CHAPTER 3: STRUCTURAL AND GAS SENSING CHARACTERISTICS OF FILMS

3.1 SPR Based Sensors Composed of Ag-YSZ Nanoparticle Films

In this study we coupled Ag with YSZ to prevent it from oxidizing and keep the SPR bands stable when being monitored in the presence of CO and H_2. Silver (Ag) nanoparticle films were deposited on glass substrates using as described in chapter 2. The substrates were cleaned with alcohol and acetone followed by drying in nitrogen. A pure silver target of 99.99% with 40 mm diameter was enclosed in a stainless vacuum chamber at 23° C. The distance between the rotating target holder, which is the ablation point, and the center of the substrate was 90 mm. This distance can be varied to change the final particle size in the films and consequently change the film quality.

Krypton fluoride (KrF) Excimer laser 248 nm (Lambda Physik Inc., LPX 201i) was set up to run at a repetition rate of 10Hz with a pulse width ~25 ns for 5 minutes, 10 minutes, and 15 minutes. The 15 minutes film is reported to have 117 nm while the 5 minutes film has 37 nm, and the 10 minutes is 76 nm thick. The thicknesses of films as measured by profilometer are presented in Figure 3.1.

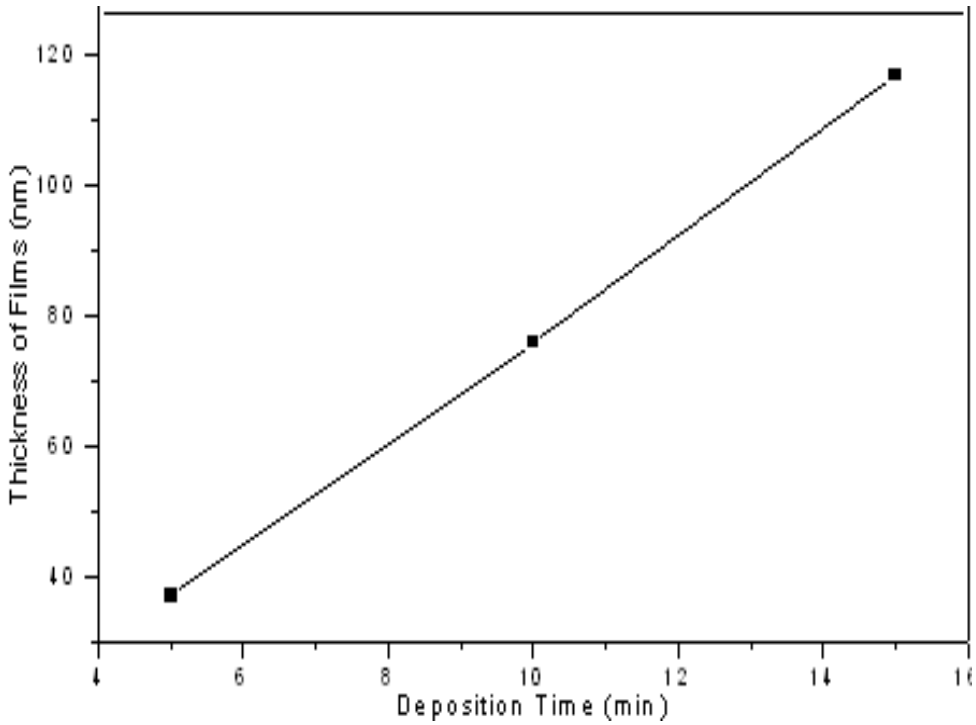

Figure 3.1 Thickness of films grown for 5, 10, 15 min. measured by profilometer

Atomic force microscopy (AFM) was performed to examine the surface morphology and the uniformity of the Ag films. Thin films of YSZ were also grown using PLD technique with a change of deposition conditions. The distance between the ablation point and the center substrate was 40 mm at temperatures of 23° C, 200° C and 400° C respectively with background vacuum in 200 mTorr. The deposition time was 30 minutes for each film. The YSZ films were first deposited on the silicon (Si) substrates and structural properties were studied using X-ray diffraction. YSZ film was deposited on glass substrates following the same procedure used for Ag deposition. The Ag films with different thicknesses were deposited on top of YSZ films. Gases of different concentrations were used. Gas flow of 100 sccm was used with mass flow controllers (MKS Inc., Type 247 controller). To make a selected gas flow through UV/vis

spectrophotometer chamber over the film under investigation for absorption change, the aluminum cell described in Chapter 2 was used effectively.

The Ag nanoparticle films were tested for different concentrations of H_2 (1%, 5% and 10% in nitrogen) and CO (100 ppm, 500 ppm and 1000 ppm in air). Surface morphology of Ag nanoparticles was studied by using atomic force microscopy. Figure 3.2-A shows the typical AFM micrograph, and Figure 3.2-B the AFM average size of Ag film.

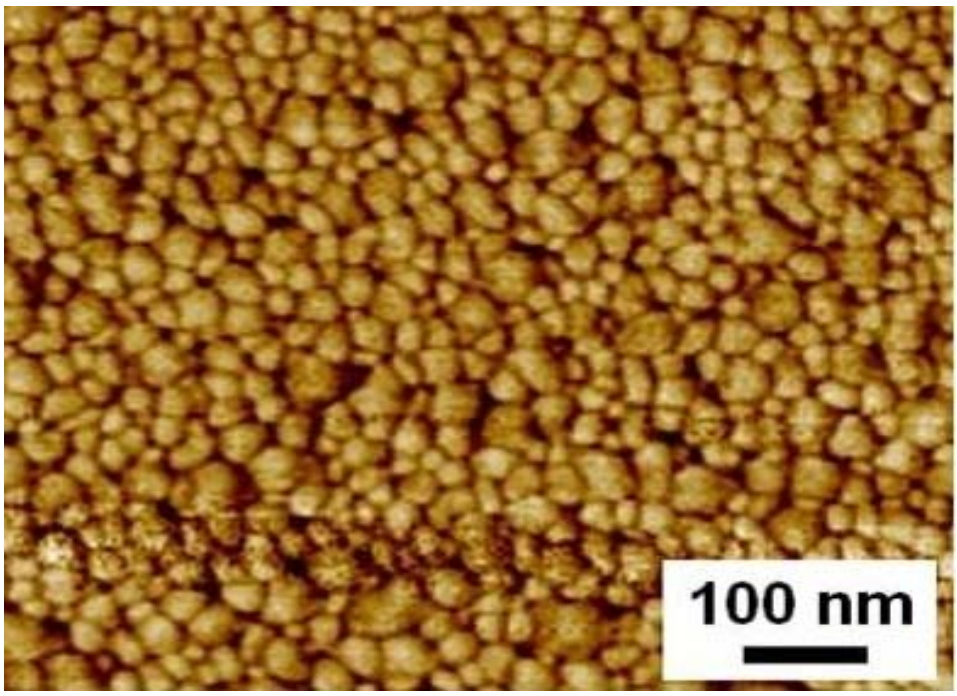

Figure 3.2.A Typical AFM micrograph of Ag film

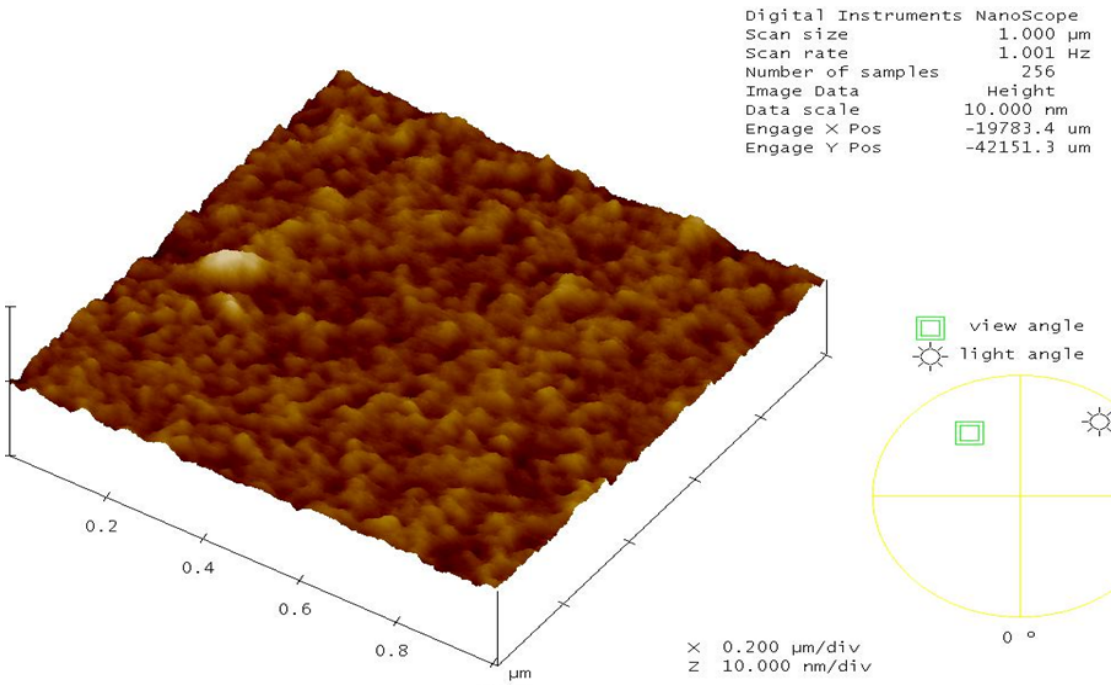

Figure 3.2.B AFM average size of Ag film (20.6nm) synthesized at RT

Ag nanoparticles with average diameter of 20 nm were synthesized for a deposition time of 10 minutes. The average grain size of the films was observed to increase with increasing the deposition time for the Ag films. X-ray diffraction (XRD) was performed to study the growth of base material YSZ. The XRD pattern for YSZ at room temperature (RT) to 400° C is shown in Figure 3.3.

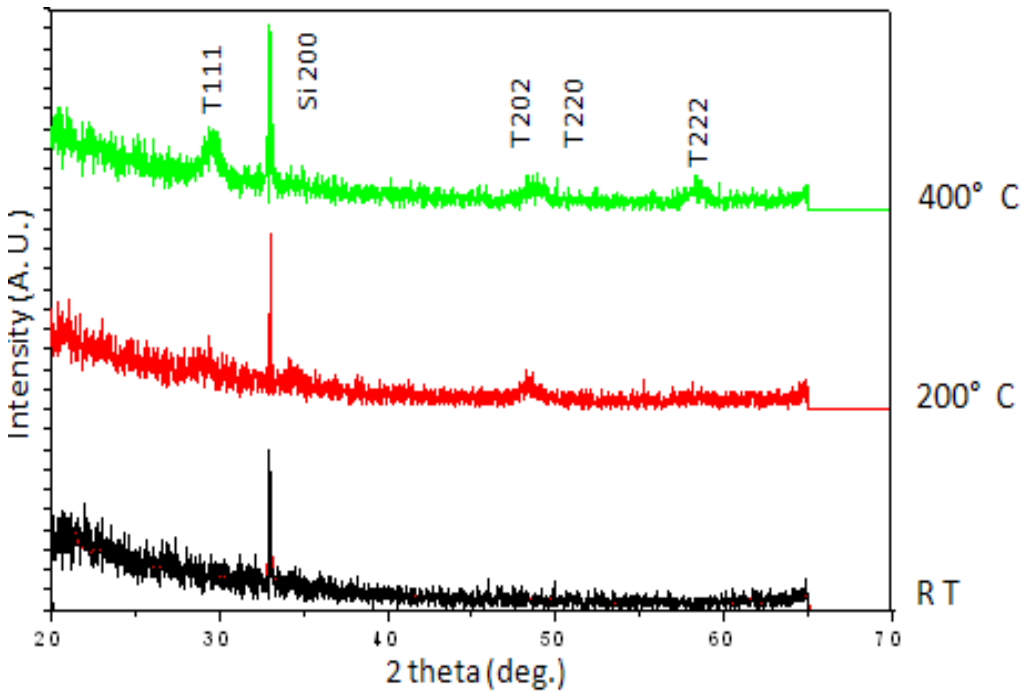

Figure 3.3 XRD pattern for YSZ films grown on Si substrates from RT - 400° C

It can be seen that at room temperature there is no remarkable YSZ peak, suggesting that the film was amorphous in such conditions. However, at 200° C for 30 minutes, the YSZ peak began to appear, and more noticeably when the substrate temperature reached 400° C, indicating that there was a sustainable crystalline improvement in the film. With such temperature increase, there is remarkable enhancement in surface morphology of YSZ film as displayed in Figure 3.4.

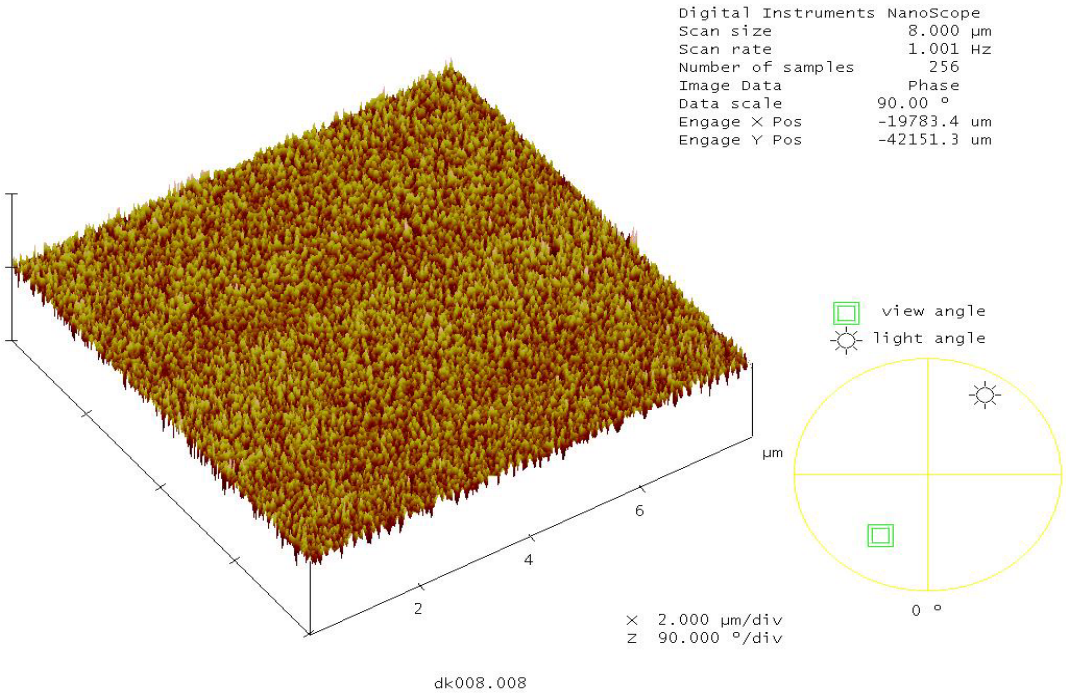

Figure 3.4 Typical AFM image of YSZ film at 400° C

Since only the YSZ film synthesized at 400° C is clearly observed to possess tetragonal structure with a strong preferential orientation along (111), it is believed that a higher substrate temperature could result in the amelioration of film crystallinity.

The XRD pattern in Figure 3-4 shows a peak of silicon emerging at approximately 35° along (200) orientation. When made on glass substrate at 400° C, the new YSZ film brought nothing but the ability to accommodate silver nanoparticles deposition for absorption monitoring and measurement in UV/vis spectrophotometer.

Surface plasmon resonance technique has been used for investigating sensing behavior of Ag films. Surface plasmon resonance on metal particles has been explained by G. Mie [35]. The SPR peak for silver is generally observed at 460 nm in our PLD grown films, as shown in Figure 3.5.

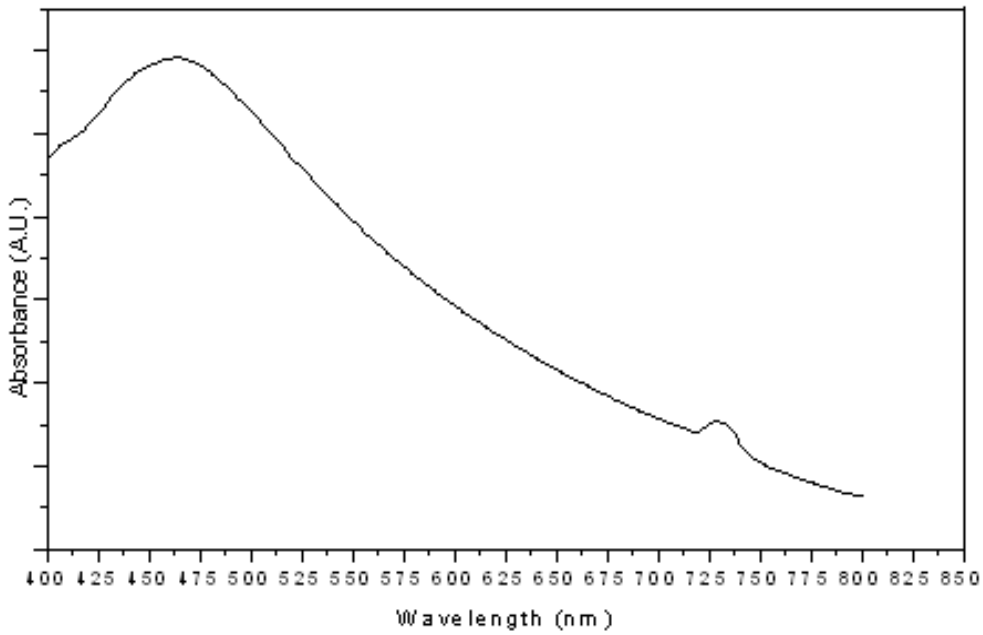

Figure 3.5 Absorption spectra of Ag film exposed to dry air at 23° C

The broadness of the peak reduces with higher grain size in the films, which can be varied by changing the parameters such as deposition temperature and the distance between the ablation point and the center substrate. SPR peak shift was observed by varying the grain size. It is believed that the growth of colloid sizes in Ag nanoparticles is the likely cause of the shift toward the longer wavelengths [36]-[37]. The absorption peak grew linearly with time of deposition, as can be observed in Figure 3.6.

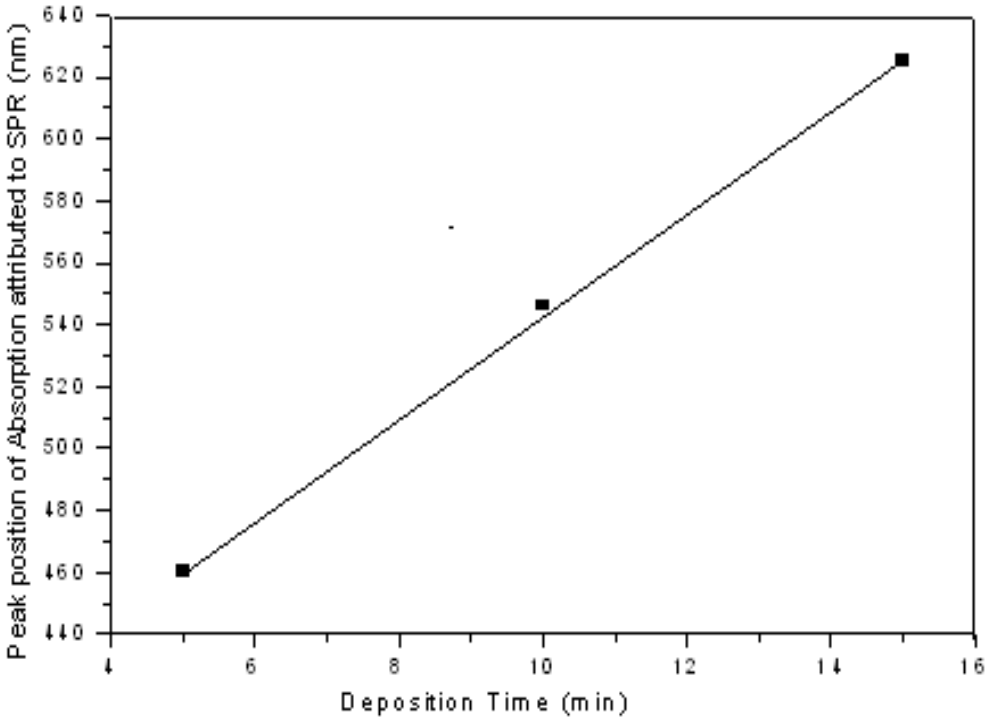

Figure 3.6 Variation of SPR peak with deposition time for Ag film

Films with short time deposition show a relatively short wavelength as opposed to those with long time deposition. For using the Ag films as gas sensors an optimized growth temperature (room temp) and distance equal to 90 mm (between the ablation point and the center substrate) were selected and all the Ag films were deposited for 5 minutes with average grain size of 20 nm.

Measuring the surface plasmon resonance in the Ag and Ag-YSZ film and determining the sensing mechanism was the main goal of this study. As preliminary stage of the investigation, the SPR proprieties of Ag and Ag-YSZ needed to be assessed before recording the measurement with a designated gas flowing over the film. As it turned out, at room temperature the SPR peak for Ag was located at ~ 460 nm, and there was no

damping in the width of the absorption spectrum. Using Ag-YSZ film for the same measurement, the peak was, as expected, at the same location, suggesting that YSZ brought no negative effect in the SPR of Ag nanoparticles. To clarity the discussion, Figure 3.7 shows the absorption spectra for YSZ-Ag film and Ag film.

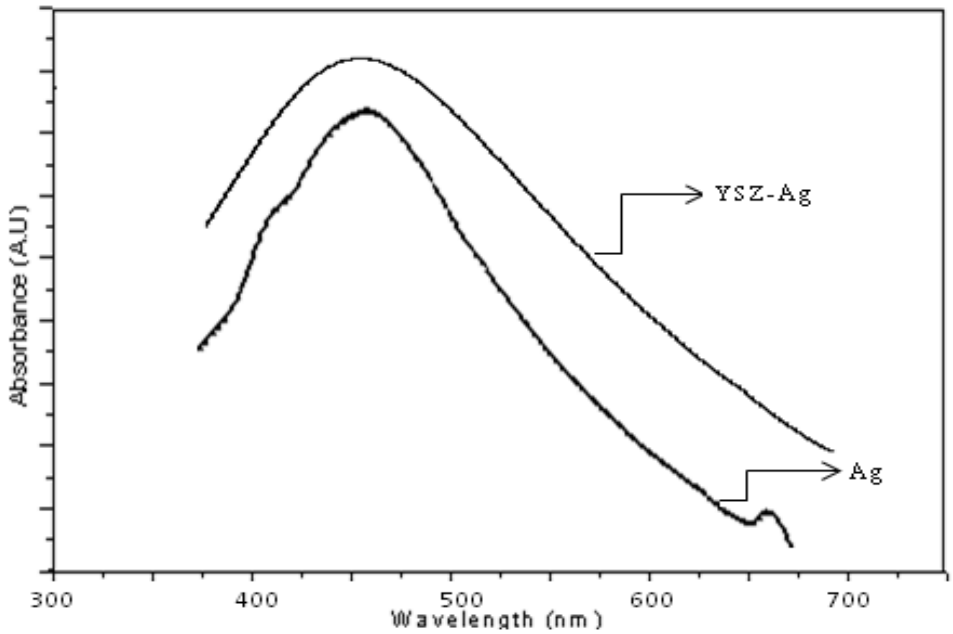

Figure 3.7 Absorption spectra of Ag and YSZ-Ag films

This result backs the idea of using YSZ as base material for Ag nanoparticle to be used as SPR based gas sensors in harsh environment in order to prevent the oxidation of Ag at higher temperature. Figure 3.8 illustrates the absorbance spectrum of Ag-YSZ nanocomposite for different gas flow at room temperature.

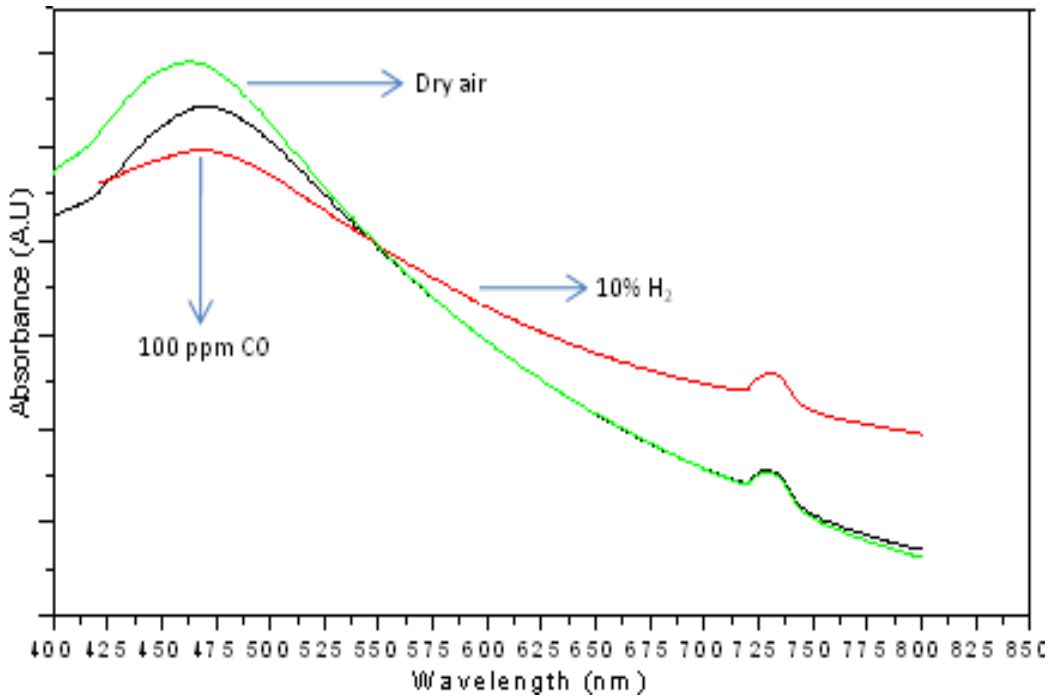

Figure 3.8 Absorption spectra of Ag-YSZ films exposed to dry air, H_2 and CO

The SPR peak was observed to shift with changing the gaseous environment around the sample, in the case of 100 ppm CO in comparison to H_2. Without any targeted gas the SPR peak was at 460 nm, while with 10% hydrogen exposure the peak rises at 478 nm, and with 100 ppm CO the SPR peak is obtained at 480 nm. Figure 3.6 shows this peak shift for the discussed gases.

The SPR band peak was observed at 492 nm for 500 ppm of CO and at 498 nm for 1000 ppm CO. In this work the gas sensor signal is defined as the percent change in SPR peak shift in absence and presence of the target. It is represented as sensor signal

$$\left(\frac{\lambda_{gas}-\lambda_{no\,gas}}{\lambda_{no\,gas}}\right)(100)$$

Here $\lambda\, gas$ and $\lambda no\ gas$ indicate wavelengths where the SPR peak was observed for the Ag nanoparticle films in absence and presence of the target gas respectively. Variations of gas sensor signal with concentration of H_2 and CO are shown in Figures 3.9 and 3.10.

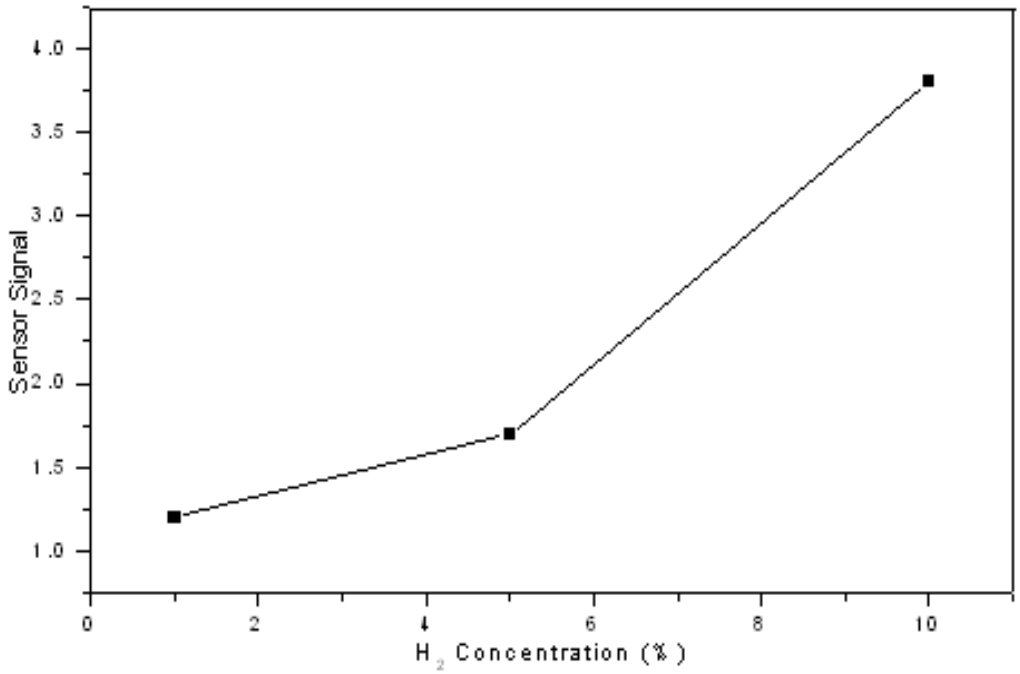

Figure 3.9 Change in sensor signal of Ag films with concentration of H_2

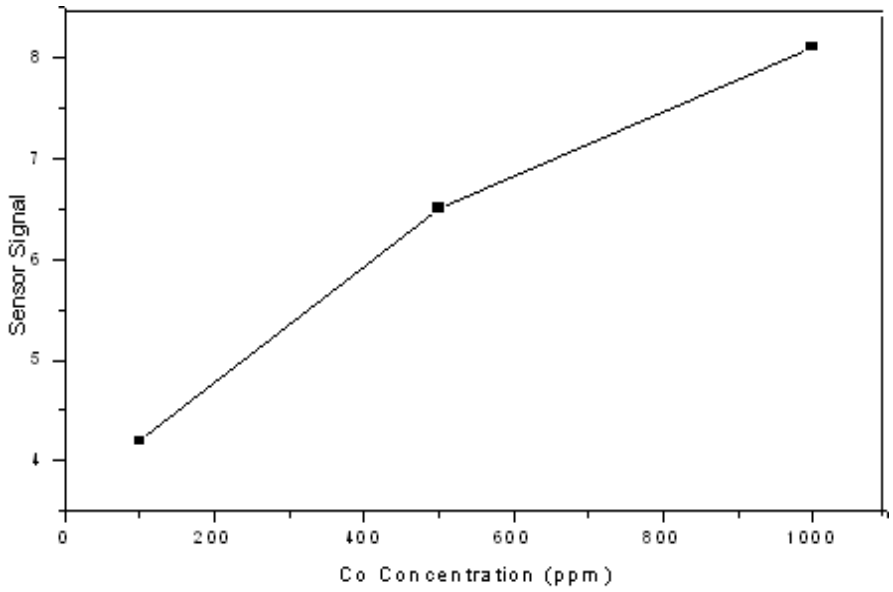

Figure 3.10 Change in sensor signal of Ag films with concentration of CO

The Ag nanoparticle films based sensors were tested for their cross-reactivity or selectivity for CO in presence of H_2 gas. For this purpose the absorption spectra with SPR peak at 478 nm was recorded in presence of 10% hydrogen. Later, in the same hydrogen environment, CO was introduced in various concentrations (100, 500 and 1000 ppm). The change in absorption spectra with SPR peak shift was recorded. The sensor signal in this case was determined as:

$$\text{Cross selectivity} = \left(\frac{\lambda_{H_2} - \lambda_{CO}}{\lambda_{H_2}}\right)(100)$$

The occurrence of SPR and LSPR depends on morphology and the nature of the sensing materials; the LSPR is considered as a predominant phenomenon in our Ag nanoparticle films. Values of 4.3, 6.7 and 8.4 for the cross-selectivity for CO in the presence of 10% H_2 are plotted in Figure 3.11.

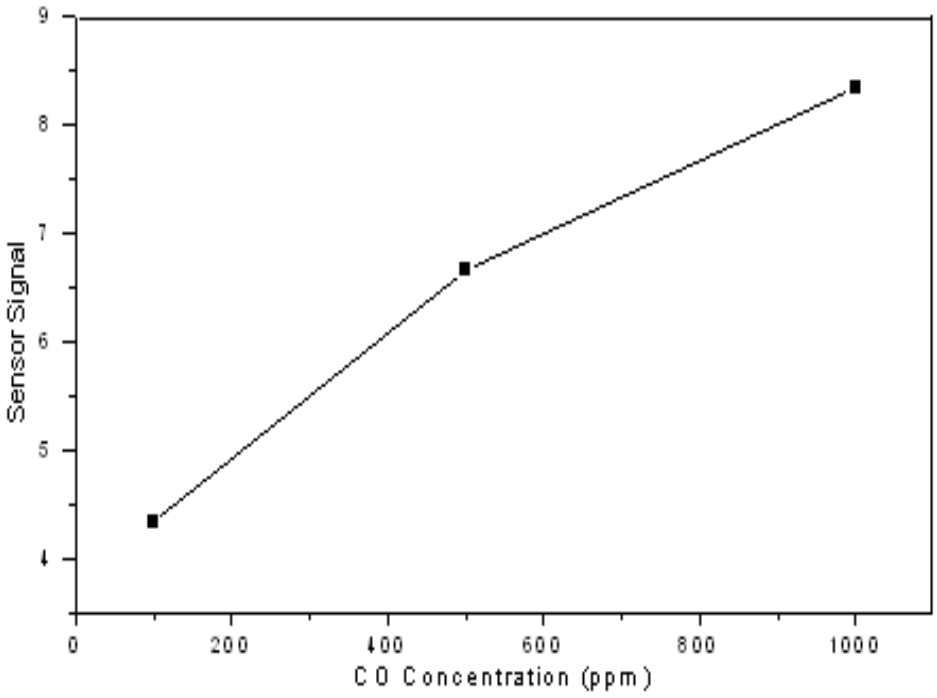

Figure 3.11 Cross-selectivity of Ag film for CO in presence of 10% H_2

3.2 SPR Based Sensors Composed of Au Nanoparticle Films

Au nanoparticle films were grown on glass substrates using PLD. Alcohol and acetone were used to remove impurities from the substrates, while nitrogen gas was to dry the substrates.. The laser beam irradiated a 99.99% pure gold target enclosed in a stainless vacuum chamber. The target-to substrate distance was 90 mm. During the deposition the background argon pressure was kept 60 m Torr. These conditions were maintained as the deposition time changed three values: 10, 15 and 20 minutes respectively in order to get films with different thickness. Table 3.1 shows the deposition conditions used for the purpose of optimizing the experiment.

Table 3.1 Gold nanoparticle films experimental conditions

Fluence	300 m/J
Target	99.99% Au
Substrate	glass
Target-to-substrate distance	90 mm
Substrate temperature (T_s)	RT to 100° C
Argon pressure (Ar_p)	60 m Torr
Deposition time	10, 15, 20 minutes

Figure 3.12 shows the thickness of gold nanoparticle films synthesized at 60 m Torr for three different deposition times. Films thickness of approximately 28, 46 and 57 nm was achieved for the deposition time of 10, 15 and 20 minutes, respectively.

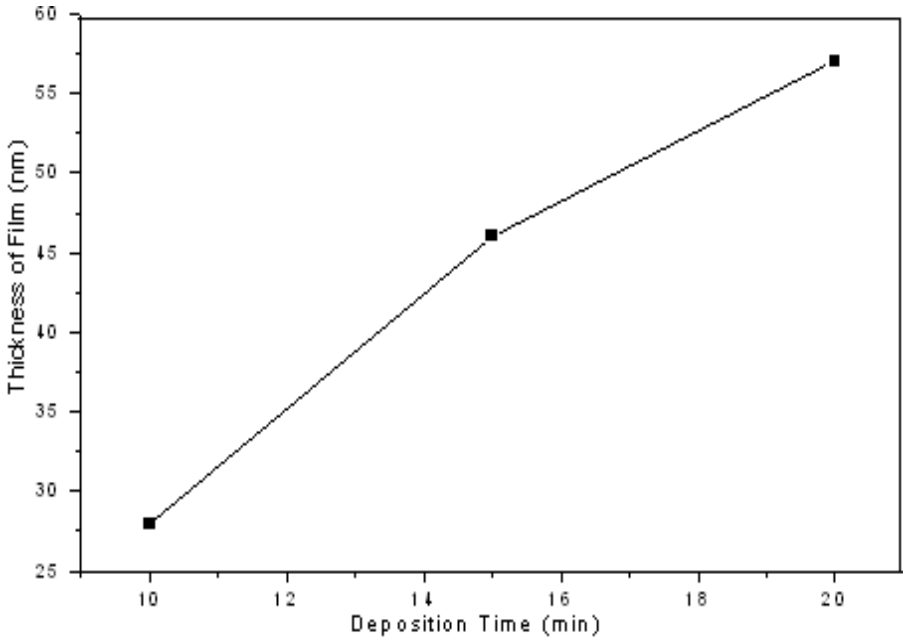

Figure 3.12 Thickness of Au films fabricated at 60 m Torr for 10, 15, 20 min.

Figures 3.13, 3.14 and 3.15 show SEM images of the three films with thicknesses as given above. The particle size in films observed and increase with increase of deposition time as seen from the SEM images.

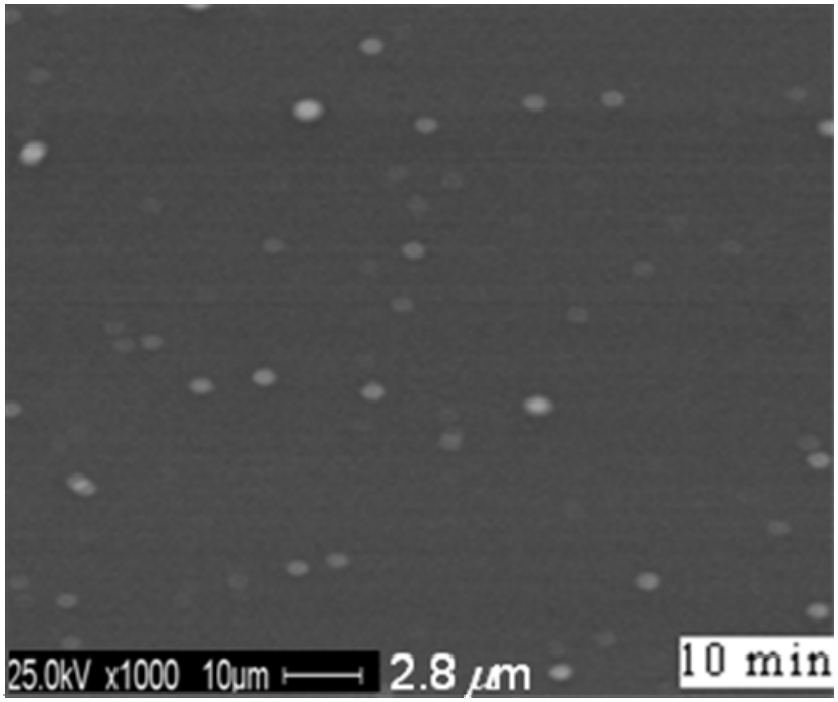

Figure 3.13 SEM image of film fabricated for 10 min.

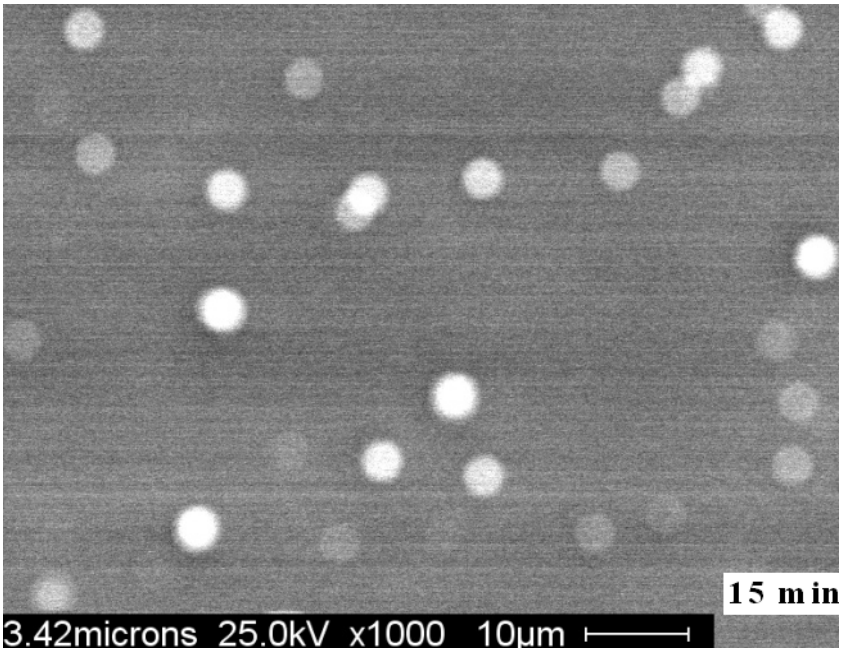

Figure 3.14 SEM image of film fabricated for 15 min.

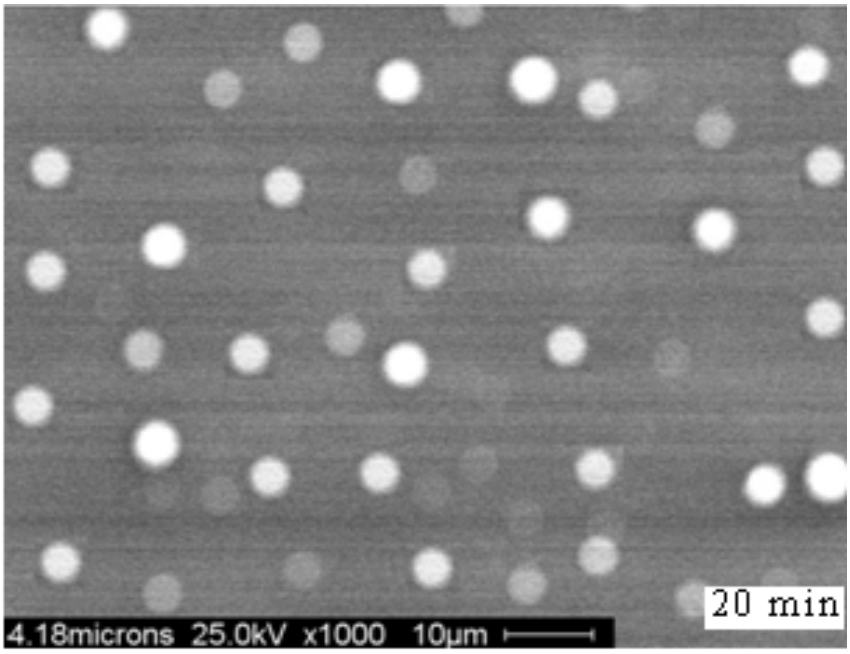

Figure 3.15 SEM image of film fabricated for 20 min.

Surface morphology study and roughness measurement were carried out using AFM. Figure 3.17 shows the AFM image for selected area (2.769 μm^2) of film.

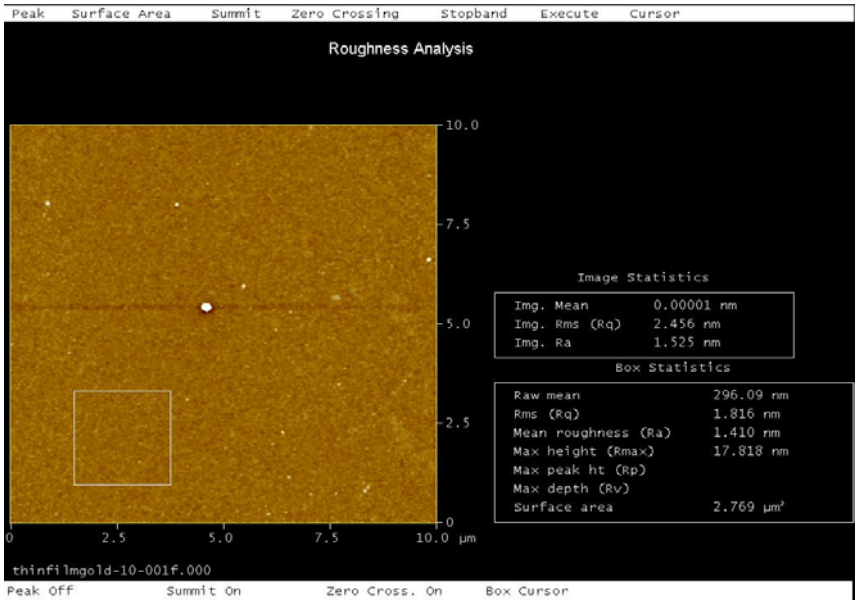

Figure 3.16 Roughness analysis of Au nanoparticle film grown for 20 min.

The typical XRD pattern (shown in Figure 3.18) for the Au film shows that the film has a crystalline Au phase with a strong preferred orientation along (111) at ~38°.

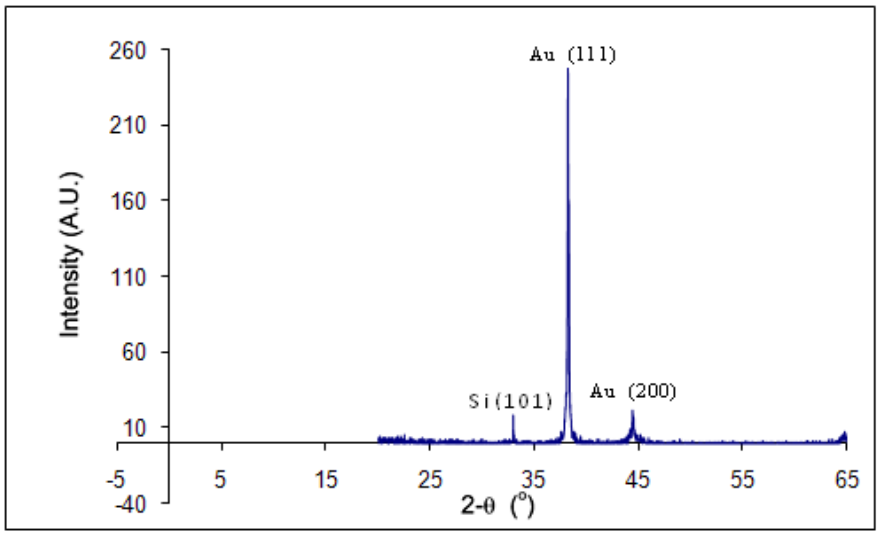

Figure 3.17 XRD pattern of Au nanoparticle film grown for 20 min.

Similar to the sensing investigation made in silver films, the sensing performance of gold nanoparticle films was accomplished by monitoring the SPR band behavior. It is observed in Figure 3.18 that the SPR peak for the gold film surface with 46 nm thickness exposed to dry air using UV/vis spectroscopy is located at 525 nm, whereas for a 10 minutes silver film in the same conditions, 460 nm is retained as peak location. Also noticeable here is the broadening of the SPR curve.

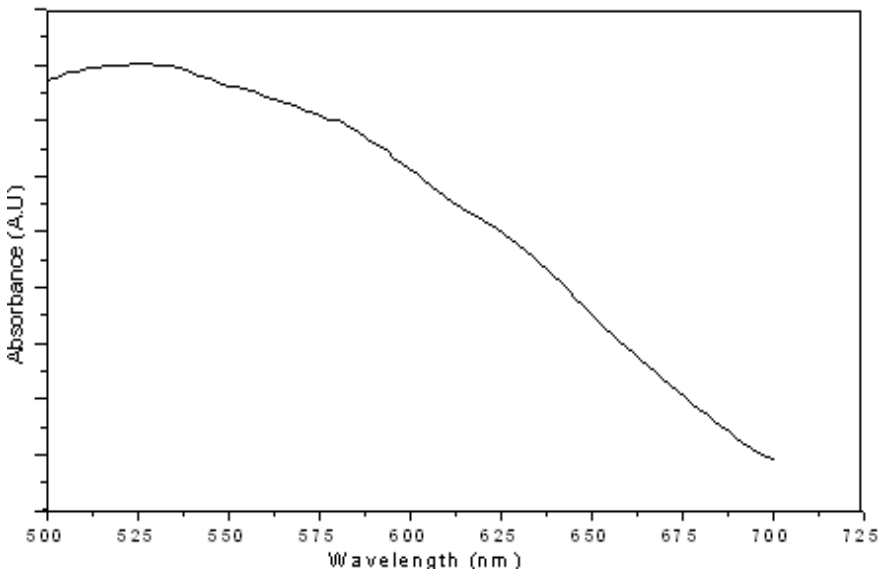

Figure 3.18 SPR peak for Au nanoparticle film exposed to dry air

When exposed to CO at two different concentrations, 100 ppm and 1000 ppm, the Au film under test shows SPR peaks at 532 nm and 539 nm respectively, shown in Figure 3.19. Figure 3.20 gives the variation in sensor signal from 100 ppm and 1000 ppm.

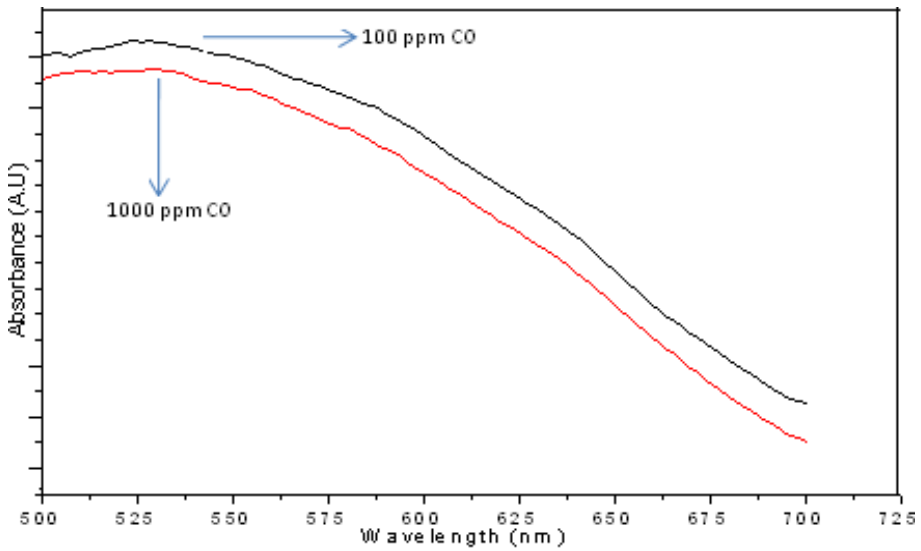

Figure 3.19 Absorption spectra of Au film exposed to CO 100 and 1000 ppm

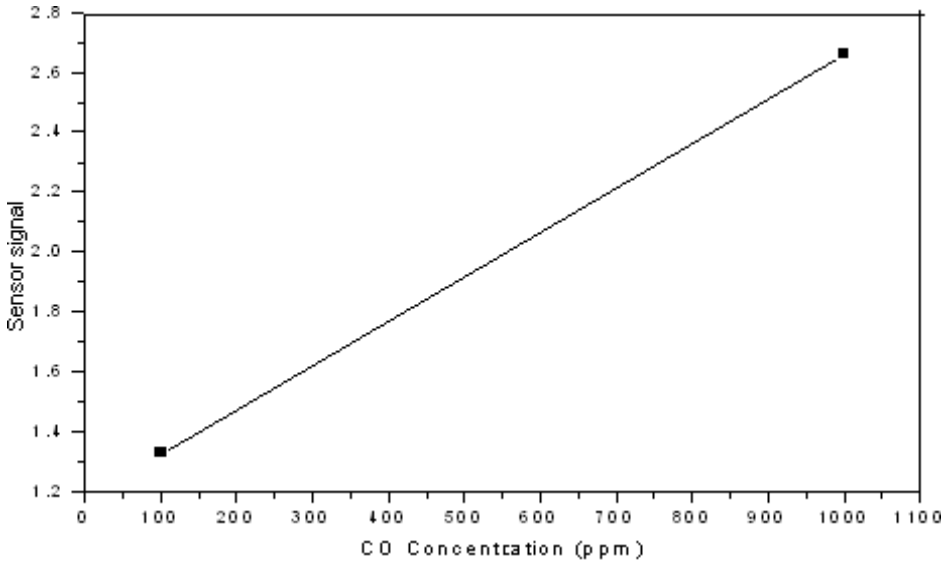

Figure 3.20 Change in sensor signal of Au film with CO 100 and 1000 ppm

The film with thickness of 57 nm was used for testing hydrogen concentration as shown in figure 3.21.

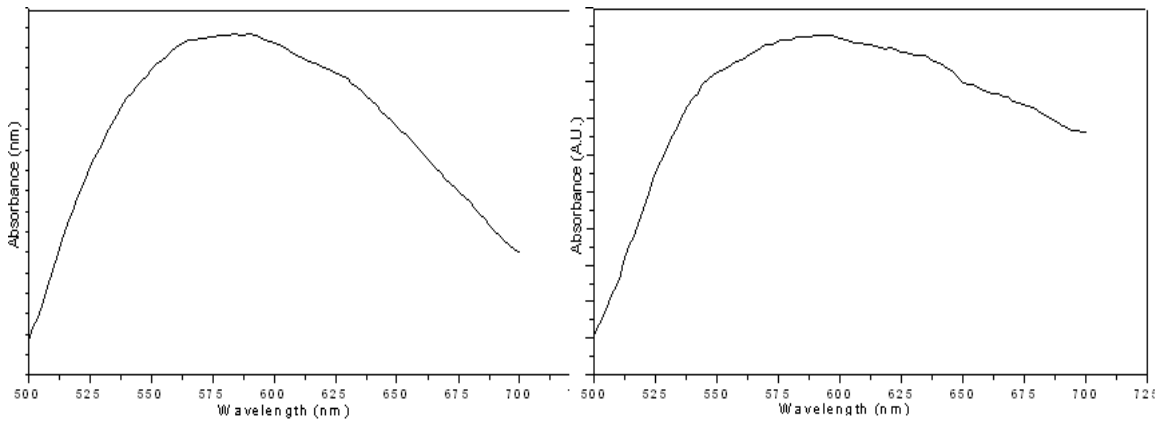

Figure 3.21 Au film (57 nm) exposed to dry air and H_2

3.3 SPR Based Sensors Composed of Ag-Cu Nanoparticle Films

In this section we study the optical properties of Ag-Cu nanocomposite film. Commercially available 99.99% pure silver and 99.99% pure copper targets were divided in half. The glass substrate used for the experimentation was also prepared in the same manner. In order to be set in the target holder the two semicircle targets were taped from the back and screwed from the side. The target was irradiated with Lambda Physik LPX 201i Excimer-laser light at wavelengths λ= 248 nm and 300 m/J as energy. The temperature in the chamber was 100° C and the background pressure was 100 m Torr. The target-to-substrate distance remained 90 mm as it was for the deposition of Ag and Au nanoparticle films. Since no weight was added to the newly assembled target, the rotation of the carousel drive remained 10 rpm. During the deposition, the repetition rate was 10 Hz. Figures 3.22 displays the silver and copper targets.

Figure 3.22 Picture of silver and copper targets

Upon completion of the deposition the film remained in the vacuum chamber for one hour until the temperature came down to 23° C. The experimental conditions are shown in Table 3.2.

Table 3.2 Ag-Cu alloy films experimental conditions

Fluence	300 m/J
Targets	99.99% Ag and Cu
Substrate	glass
Target-to-substrate distance	90 mm
Substrate temperature (T_s)	100° C
Argon pressure (Ar_p)	100 m Torr
Deposition time	20, 25, 30 minutes

Figure 3.23 shows film thickness as function of ablation time. As in the previous film thickness investigations, the thickness of Ag-Cu nanoparticle films increased with ablation time. For the 20, 25 and 30 minutes films, 112, 141 and 165 nm were found as thickness measurements using profilometer.

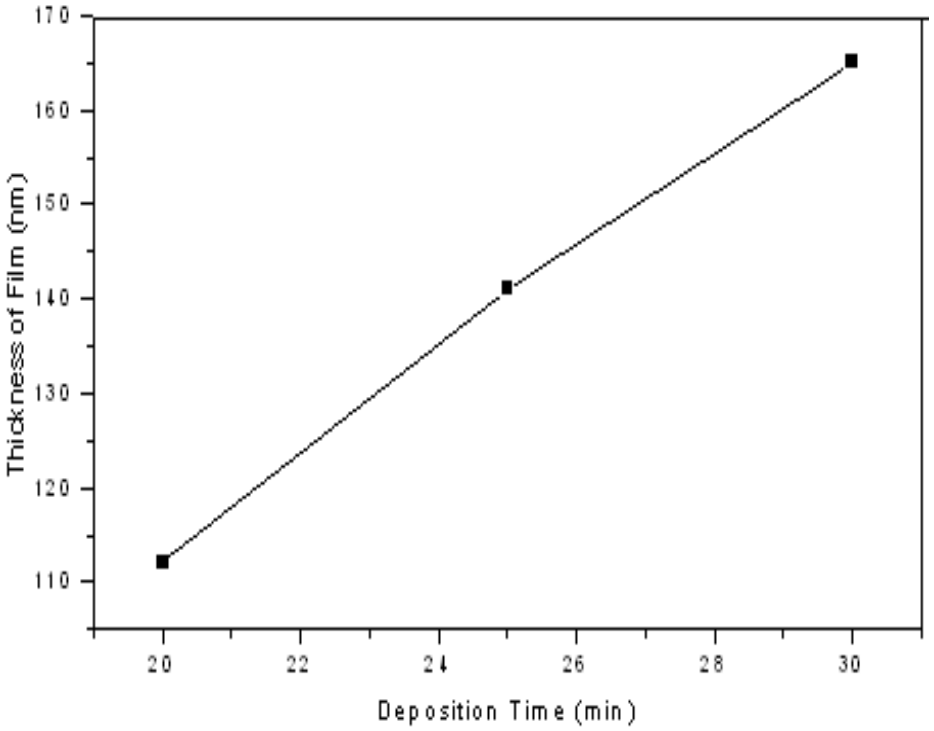

Figure 3.23 Thickness of Ag-Cu films fabricated at 100 m Torr for 20, 25 and 30 min.

The 20, 25 and 30 minutes ablation time for Ag-Cu is an increase from the 10, 15, and 20 minutes time used for Au. This provokes thought for possible reasons: melting point could be one.

To investigate the microstructure of Ag-Cu film, its deposition was made in a silicon wafer following the conditions given above. XRD analysis shows, as in Figure 3.24, that the structure of the deposited film contained a crystalline silver–copper phase with a strong preferential orientation along (111) at ~38° for silver. Copper, however, had a (200) orientation at ~44° while silicon orientation was (101) at ~33°.

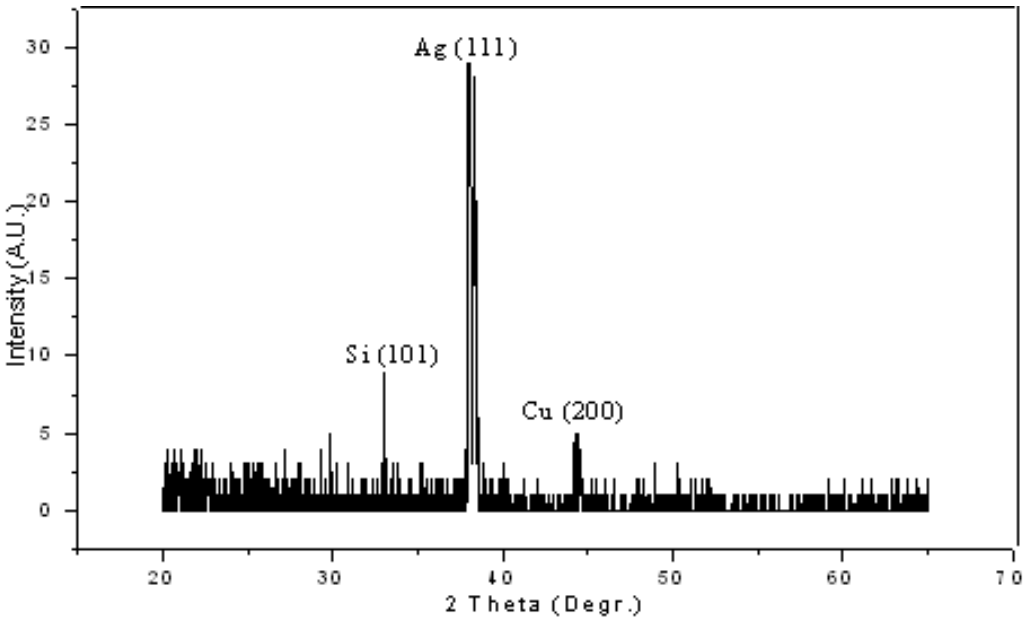

Figure 3.24 XRD pattern for Ag-Cu alloy film

Figure 3.25 shows absorption spectra of Ag-Cu exposed to dry air with 581 nm as peak location. As can be seen, the curve covers almost the entire visible region. The higher conductivity of copper, compared to silver, seems to influence the increase in broadness.

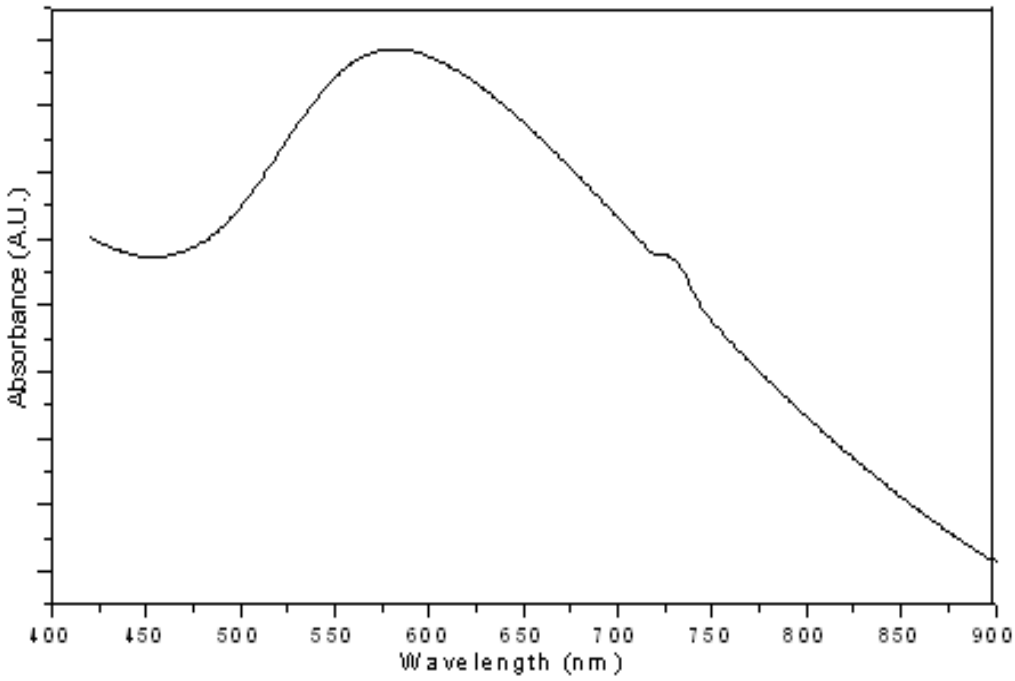

Figure 3.25 Absorption spectra of Ag-Cu film exposed to dry air at 23° C

Ag-Cu alloy nanoparticle films have what it takes to make a more sensitive SPR based sensor. Figure 3.29 shows absorption spectra of Ag-Cu film exposed to dry air, 10 % H_2 and CO at 100 ppm with 581, 611 and 623 nm respectively. It is believed, based on the pattern of the previous analysis, that the higher the concentration the longer the wavelength at which the absorption peak attributed to SPR is located.

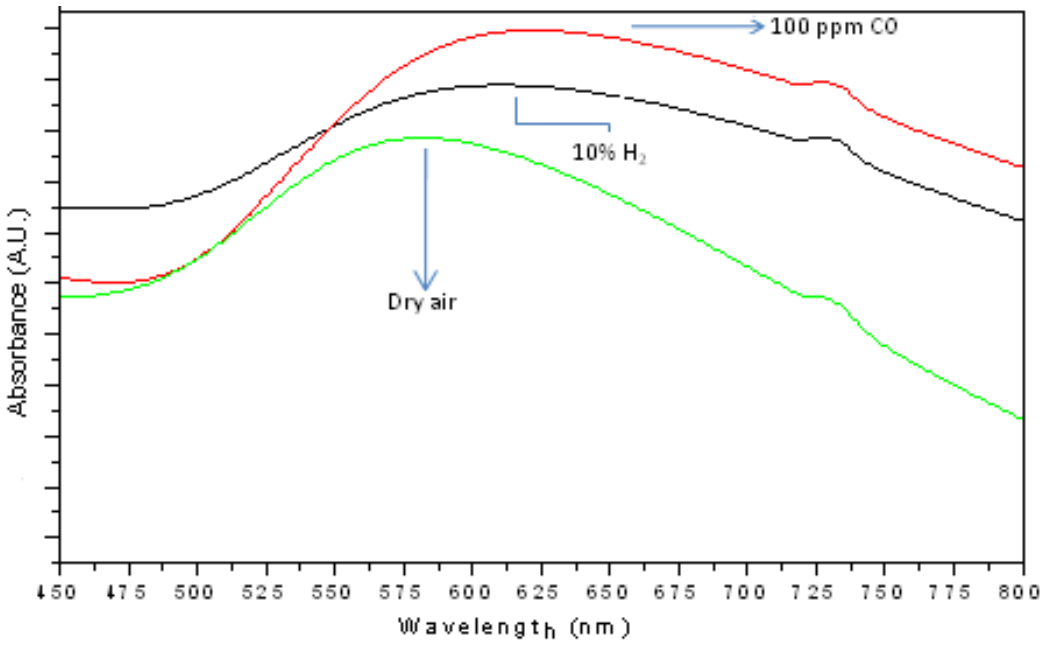

Figure 3.26 Absorption spectra: Ag-Cu film exposed to dry air, 10% H_2, CO 100 ppm

The sensing signal calculation was estimated by percentage change in wavelength for SPR shift in the same manner we had done all along. As it turned out, 5.16 was recorded as sensing signal when the Ag-Cu nanoparticle film was exposed to 10% H_2 and 7.22 at the exposure to CO (100 ppm). This result puts Ag-Cu alloy film at the top, when compared with Ag and Au films, for H_2 and CO detection at the indicated concentration and under standard conditions.

From the preceding analysis and results it might be tempting to conclude that surface plasmon resonance based sensors bring nothing but perfection to sensing technology. A close and careful look, however, at the functionality of SPR sensors yields to the conclusion that SPR based sensors have issues like other types of sensors. The first issue associated with SPR sensors is related to the infiltration of random errors

which are the statistical fluctuations in the measured data due to the precision limitations of the sensor system. These errors are generated by instrument components such as light source and detector capability. Progress has been made to improve light efficiency in the past. Quartz tungsten halogen lamp for example shows high stability but fluctuations in the light source remains an issue in SPR based sensors. To solve this issue, development of detectors of light intensity with a higher signal-to-noise ratio could be the solution [38]-[39]. The same assessment can be made regarding the limit of detection (LOD) in SPR based sensors. It was determined in the course of this study that the gases in concentration like 1% for H_2 and 100 ppm for CO can be sensed. The reasons for these delays could have been the quality of the films or the instability in the cell-testing assembly.

CHAPTER 4: CONCLUSION AND FUTURE WORK

4.1 Conclusion

This study has demonstrated the detection of CO and H_2 in low concentrations using SPR phenomenon. The results suggest that Ag-YSZ, Au and Ag-Cu nanoparticle films, which served for test sensing devices, exhibit relatively high sensitivity with reference to the shift in peak position and the narrowing of SPR band. The overall results put Ag nanoparticle films at the top when compared to that of silver as far as sensitivity is concerned. However, the sensing performance observed in silver-copper alloy film indicates that promising sensing material might be coming from the combination of different materials rather than from single ones, as shown in Table 4.1 and Figures 4.1 and 4.2.

Table 4.1 H_2 and CO sensor signals comparisons for Ag, Au and Ag-Cu films

Sensor sensing element	Target gas & concentration	Sensor signal
Silver nanoparticle film	H_2 (10%)	3.9
Silver nanoparticle film	CO (100 ppm)	4.3
Gold nanoparticle film	H_2 (10%)	1.3
Gold nanoparticle film	CO (100 ppm)	1.6
Silver-copper nonocomposite film	H_2 (10%)	5.1
Silver-copper nonocomposite film	CO (100 ppm)	7.2

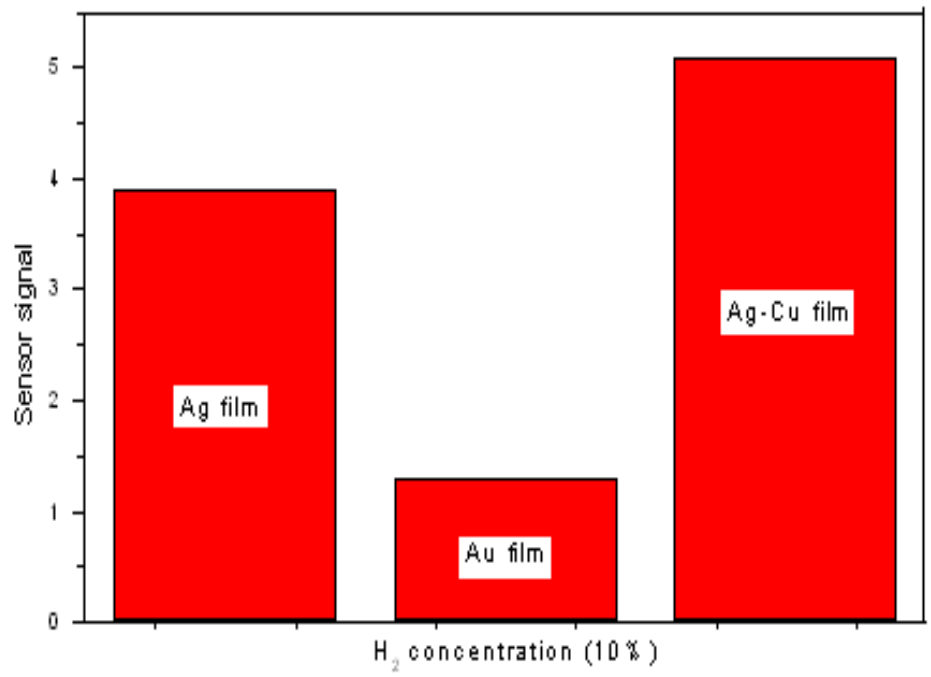

Figure 4.1 H_2 sensor signal comparison for Ag, Au and Ag-Cu films

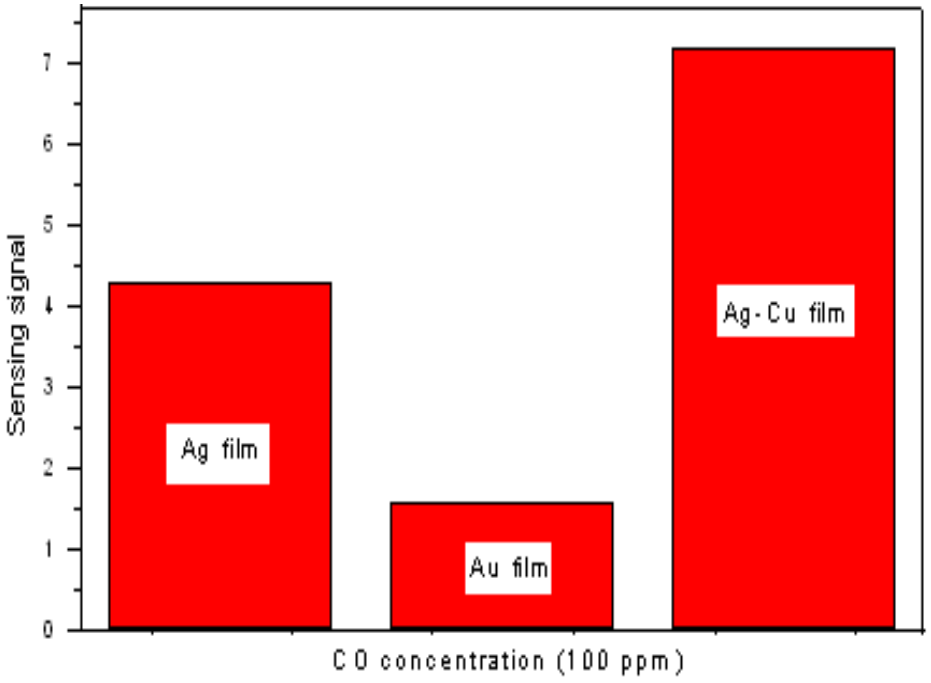

Figure 4.2 CO 100 ppm sensor signal comparison for Ag, Au and Ag-Cu films

It was also demonstrated, in the course of the experimental procedure, that film sensitivity depends for the most part on the refractive index of the medium, which makes it possible to predict the signal range and sensitivity level. Other variables, such as particle size and shape, thickness along with film morphology, grain size and even the distance particle-to-particle, do play a relevant role in the sensing mechanism as well. The results and discussion yield to the following comments.

Compared with metal oxide-based sensors, a promising way of using UV/vis spectrophotometer to detect the presence of CO and H_2 in standard conditions is initiated in this study. However, the actual configuration of the sensor requires more research time and resources to find an effective technique to reduce the noise in the system, which could have been generated from the instability of the film holder or most likely from the systematic control of gas flow over the film under investigation.

4.2 Future Work

Further research on the following topics could significantly enhance the range of sensitivity observed in the films:

1) Other gases like NH_4, and NO_x, H_2S, Ethanol vapors can be tested for SPR based gas sensing.
2) Use alloy and composite films to improve the gas sensor signal and selectivity.

REFERENCES

[1] D. Kitenge, R. Joshi, M. Hirai and A. Kumar. Nanostructured Silver Films for Surface Plasmon Resonance Based Gas Sensors. Accepted by Institute of Electrical and Electronics Engineers (IEEE). 2009.

[2] P. Tobiska, O. Hugon, A. Trouillet and H. Gagnaire. An Integrated Optic Hydrogen Sensor Based on SPR on Palladium. Sensors and Actuators B, vol. 74, pp. 168-172. 2001.

[3] N. Yamazoe. Toward Innovations of Gas Sensor Technology. Sensors and Actuators B, vol. 108**,** pp. 2–14. 2005.

[4] A. Rothschild and Y. Komen. The Effect of Grain Size on the Sensitivity of Nanocrystalline Metal-oxide Gas Sensors. Journal of Applied Physics, vol. 95, p. 6374. 2004.

[5] C. Xu, J. Tamaki, N. Miura and N. Yamazoe. Grain Size Effects on Gas Sensitivity of Porous SnO_2-based Elements. Sensors and Actuators B, vol**.** 3**,** pp. 147–155. 1991.

[6] K. Yoshioka, T. Tanihira, K. Shinnishi and K. Kaneyasu. Development of Extremely Small Semiconductor Gas Sensor. Chemical Sensors, vol. 23, pp. 16–18. 2007.

[7] J. Homola, S.S. Yee and G. Gauglitz. Surface Plasmon Resonance Sensors: Review. Sensors and Actuators B, vol. 54, pp. 3-15. 1999.

[8] J. Homola. *Surface Plasmon Resonance Based Sensors.* Springer-Verlag Berlin Heidelberg. 2006.

[9] B. Liedberg, C. Nylander and I. Lundstrom. Surface Plasmon Resonance for Gas Detection and Biosensing. Sensors and Actuators B, vol. 4, pp. 299-304. 1983.

[10] R. L. Rich and D. G. Myszka. Why You Should be Using More SPR Biosensor Technology. Drug Discovery Today: Technology, vol. 1, No. 3, pp. 3001-3008. 2004.

[11] C. Kang, S. W. Lee, T. H. Park and S. J. Sim. Performance Enhancement of Real-time Detection of Protozoan Parasite Cryptosporidium Oocyst by a Modified Surface Plasmon Resonance (SPR) Biosensor. Enzyme and Microbial Technology, vol. 39, pp. 387–390. 2006.

[12] R. W. Cohen, G. D. Cody, M. D. Coutts, and B. Abeles. Optical Properties of Granular Silver and Gold Films. Physics Review B, vol. 8, p. 3689. 1973.

[13] T. Wagner. *Thin Film Science.* Max-Plank-Institut fur Metallforschung, 70174 Stuttgart, Germany, from http://www.mpg.de/pdf/europeanWhiteBook/wb_materials_196_200.pdf

[14] Z. Konstantinovic, M. Garcia del Muro, M. Varela, X. Batlle and A. Labarta. Metallic Nanoparticles Embedded in an Insulator Matrix: Growth Mechanisms, Magnetic and Transport Properties. XVII Symposium on Condensed Matter Physics, Vrsac – Serbia, SFKM. 2007.

[15] M. F. Al-Kuhaili, S. M. A. Durrani and I. A. Bakhtiari. Carbon Monoxide Gas-sensing Properties of CeO_2–ZnO Thin Films. Applied Surface Science, vol. 255, p. 3033–3039. 2008.

[16] J. Homola. *Surface Plasmon Resonance Based Sensors*

[17] L. B. Scaffardi and J. O. Tocho. Size Dependence of Refractive Index of Gold Nanoparticles. Nanotechnology**,** vol. 17, pp. 1309-1315. 2006.

[18] J. Homola, S. S. Yee and G. Gauglitz. Surface Plasmon Resonance Sensors

[19] J. G. Speight. *Lange's Handbook of Chemistry*. New York: McGraw Hill. 2005.

[20] R. D. Hudson. *Infrared System Engineering.* New York: Wiley. 1969.

[21] S. A. Ramakrishna. *Physics and Applications of Negative Refractive Index Materials*. London: CRC Press. 2009.

[22] S. B. Ogale. Thin Films and Heterostructures for Oxide Electronics. New York: Springer Science + Business Media. 2005.

[23] G. Mie. Contributions to the Optics Turbid Media, Especially Colloidal Metal Solutions. Annalen der Physik, vol. 330, p. 377-445. 1908.

[24] C. E. Rayford II, G. Schatz and K. Shuford. Optical Properties of Gold Nanospheres. Nanoscape, vol. 2, p. 27-33. 2005.

[25] J. Homola. *Surface Plasmon Resonance Based Sensors*

[26] J. Homola. *Surface Plasmon Resonance Based Sensors*

[27] Y. Saito, H. Kumagai and S. Suganamata. Coloration of Quartz by Metal-Ion Implantation. Japanese Journal of Applied Physics, vol. 24, pp. 1115-1116. 1985.

[28] Y. Saito, D. Y. Shang, R. Kitsutaka and A. Kitahara. Optical Properties of Cu-implanted $LiNbO_3$

[29] M. D. McMahon, R. Lopez, H. M. Meyer III, L. C. Feldman and R. F. Haglund, Jr. Rapid Tarnishing of Silver Nanoparticles in Ambient Laboratory Air. Journal of Applied Physics, vol. 80, pp. 915-921. 2005.

[30] G. Sirinakis, R. Siddique, I. Manning, P. H. Rogers, and M. A. Carpenter. Development and Characterization of Au-YSZ Surface Plasmon Resonance Based Sensing Materials: High Temperature Detection of CO_2. The Journal of Physical Chemistry B, vol. 110, p. 13508. 2006.

[31] P. H. Rogers, G. Sirinakis and M. A. Carpenter. Plasmonics Based Detection of NO_2 in a Harsh Environment

[32] G. K. Hubler. Pulsed Laser Deposition. MRS Bulletin, vol. XVII, No. 2, pp. 26-29. 1992.

[33] G. K. Hubler. Pulsed Laser Deposition.

[34] T. Owen. *Fundamentals of UV-visible Spectroscopy*. Germany: Hewlett-Packard Company. 1996.

[35] G. Mie. Contributions to the Optics Turbid Media, Especially Colloidal Metal Solutions

[36] Y. Saito, Y. Imamura and A. Kitahara. Optical Properties of YSZ Implanted with Ag Ions. Nuclear Instruments and Methods in Physics Research, Section B: Beam Interactions with Materials and Atoms, vol. 206, pp. 272-276. 2003.

[37] S. Link and M. A. El-Sayed. Size and Temperature Dependence of the Plasmon Absorption of Colloidal Gold Nanoparticles. Journal of Physical Chemistry, vol. 103, pp. 4212-4217. 1999.

[38] J. Homola. *Surface Plasmon Resonance Based Sensors*

[39] M. Piliarik and J. Homola. Surface Plasmon Resonance (SPR) Sensors: Approaching Their Limits? Optics Express, vol. 17, No. 19, pp. 16505-16517. 2009.

BIBLIOGRAPHY

Al-Kuhaili, M. F., Durrani, S. M. A. and Bakhtiari, I. A. 2008. Carbon Monoxide Gas-sensing Properties of CeO_2–ZnO Thin Films, Applied Surface Science, vol. 255, pp. 3033–3039.

Bassim, N. D., Schenck, P. K., Donev, E. U., Heilweil, E. J., Cockayne, E., Green, M. L. and Feldman, L. C. 2007. Effects of Temperature and Oxygen Pressure on Binary Oxide Growth Using Aperture-controlled Combinatorial Pulsed-laser Deposition, Applied Surface Science, vol. 254, pp. 785–788.

Binnig, G., Quate, C. F. and Gerber, Ch. 1986. Atomic Force Microscope, Physical Review Letters, vol. 56, pp. 930-933.

Castro-Rodrıguez, R., Reyes-Coronado, D., Iribarren, A., Watts, B. E., Leccabue, F. and Pena, J. L. 2005. Correlation Between Target–substrate Distance and Oxygen Pressure in Pulsed Laser Deposition of Complex Oxide Thin Films, Applied Physics A, vol. 81, pp. 1503–1507.

Cheng Chang, C. 1997. Effect of Annealing on $PbTiO_3$ Thin-film Quality Improvement, Thin Solid Films, vol. 311, pp.304–309.

Cheung, J. and Horwitz, J. 1992. Pulsed Laser Deposition History and Laser-target Interactions, MRS Bulletin, vol. XVII, No. 2, pp. 30-36.

Chrisey, D. B. and Hubler, G. K. (eds.). 1994. *Pulsed Laser Deposition of Thin Films*, New York: John Wiley & Sons.

Chui, B. W. 1999. *Microcantilevers for Atomic Force Microscope Data Storage*, Boston: Kluwer Academic Publishers.

Cohen, R. W., Cody, G. D., Coutts, M. D. and Abeles, B. 1973. Optical Properties of Granular Silver and Gold Films, Physics Review B, vol. 8, p. 3689.

Depaz, M. 2007. Zinc Oxide Thin Films, Master's Thesis in Mechanical Engineering, University of South Florida.

Duparré, A., Kaiser, N. and Heaton, M. G. 2004. Using Atomic Force Microscopy (AFM) for Engineering Low-scatter Thin Film Optics, from http://www.veeco.com/pdfs/appnotes/AN21_Optics_081904_RevA1_9.pdf

Eggins, B. 2007. *Chemical sensors and biosensors*, Chichester, West Sussex, England.

Gagnon, Steve maintains the page, Jefferson Lab, Science Education. http://education.jlab.org/itselemental/ele079.html

Gagnon, Steve maintains the page, Jefferson Lab, Science Education. http://education.jlab.org/itselemental/ele079.html

Gagnon, Steve maintains the page, Jefferson Lab, Science Education. http://education.jlab.org/itselemental/ele079.html

Guenther, K. H., Loo, B., Burns, D., Edgell, J., Windham, D. and Muller, K-H. 1989. Microstructure Analysis of Thin Films Deposited by Reactive Evaporation and by Reactive Ion-plating, The Journal of Vacuum Science and Technology A, vol. 7, pp. 1436-1445.

Gupta, A. "Novel Pulsed Laser Deposition Approaches", citing Geohegan, D. B. 1991, Materials Research Society Symposium Proceedings, vol. 201, pp 557-562 in Chrisey, D. B. and Hubler, G. K. (eds.) 1994, *Pulsed Laser Deposition of Thin Films*, New York: John Wiley & Sons.

Hearle, J. W. S., Sparrow, J. T. and Cross, P. M. 1972. *The Use of the Scanning Electron Microscope.* Oxford, New York: Pergamon Press.

Hellmann, R., Drake, B. and Kjoller, K. (Y. K. Kharaka and A. S. Maest, eds.). 1992. Using Atomic Force Microscopy to Study the Structure, Topography and Dissolution of Albite Surfaces, Water-Rock Interaction WRI-7, pp.149-152.

Homola, J. 2006. *Surface Plasmon Resonance Based Sensors*, Springer-Verlag Berlin Heidelberg.

Homola, J., Yee, S. S. and Gauglitz, G. 1999. Surface Plasmon Resonance Sensors: Review, Sensors and Actuators B, vol. 54, pp. 3-15.

Hubler, G. K. 1992. Pulsed Laser Deposition, MRS Bulletin, vol. XVII, No. 2, pp. 26-29.

Hudson, R. D. 1969. *Infrared System Engineering,* New York: Wiley.

Ito, S., Fujioka, H., Ohta, J., Sasaki, A., Liu, J., Yoshimoto, M., Koinuma, H. and Oshima, M. 2003. Low-temperature Growth of AlN on Nearly Lattice-matched MnO Substrates, Applied Surface Science, vol. 216, pp. 508–511.

Jiang, T., Hall, N., Ho, A. and Morin, S. 2005. Quantitative Analysis of Electrodeposited Thin Film Morphologies by Atomic Force Microscopy, Thin Solid Films, vol. 471, pp. 76-85.

Kakudo, M. and Kasai, N. 1972. *X-Ray Diffraction by Polymers*, N.Y. Elsevier Science.

Kakudo, M. and Kasai, N. 1968. X-RAY Diffraction by Polymers, American Elsevier Publishing Company, Inc, N.Y.

Kang, C., Lee, S. W., Park, T. H. and Sim, S. J. 2006. Performance Enhancement of Real-time Detection of Protozoan Parasite Cryptosporidium Oocyst by a Modified Surface Plasmon Resonance (SPR) Biosensor, Enzyme and Microbial Technology, vol. 39, pp. 387–390.

Kitenge, D., Joshi, R., Hirai, M. and Kumar, A. 2009. Nanostructured Silver Films for Surface Plasmon Resonance Based Gas Sensors, accepted by Institute of Electrical and Electronics Engineers (IEEE).

Kjendal, D. L. 1995. Design and Implementation of Physical Vapor and Chemical Vapor Assisted Thin Film Deposition Systems and the Study of Laser Processed Polymetric Material, Master Thesis, University of South Alabama, December.

Konstantinovic, Z., Garcia del Muro, M., Varela, M., Batlle, X. and Labarta, A. 2007. Metallic Nanoparticles Embedded in an Insulator Matrix: Growth Mechanisms, Magnetic and Transport Properties, XVII Symposium on Condensed Matter Physics, Vrsac – Serbia, SFKM.

Liedberg, B., Nylander, C. and Lundstrom, I. 1983. Surface Plasmon Resonance for Gas Detection and Biosensing, Sensors and Actuators B, vol. 4, pp. 299-304.

Link, S. and El-Sayed, M. A. 1999. Size and Temperature Dependence of the Plasmon Absorption of Colloidal Gold Nanoparticles, Journal of Physical Chemistry, vol. 103, pp. 4212-4217.

McMahon, M. D., Lopez, R., Meyer III, H. M., Feldman, L. C. and Haglund, Jr., R. F. 2005. Rapid Tarnishing of Silver Nanoparticles in Ambient Laboratory Air, Journal of Applied Physics, vol. 80, pp. 915-921.

McPherson, A. 2003. *Introduction to Macromolecular Crystallography, Anewandte Chemie International Edition*

Mie, G.1908. Contributions to the Optics Turbid Media, Especially Colloidal Metal Solutions, Annalen der Physik, vol. 330, pp. 377-445.

Oatley, C. W. 1972. *The Scanning Electron Microscope*, London: Cambridge University Press.

Ogale, S. B. 2005. Thin Films and Heterostructures for Oxide Electronics, New York: Springer Science + Business Media.

Onuki, T. and Kuwano, H. 2009. Low Resistive Copper Films Deposited Using the Ion Beam Sputtering Method with an Ultra-high Purity Target, Journal of Micromechanics and Microengineering, vol. 19, pp 1-6.

Owen, T. 1996. *Fundamentals of UV-visible Spectroscopy*, Germany: Hewlett-Packard Company.

Patskovsky, S., Kabashin, A. V., Meunier, M. and Luong, J. H. T. 2003. Properties and Sensing Characteristics of Surface-plasmon Resonance in Infrared Light, Journal of the Optical Society of America, vol. 20, Issue 8, pp. 1644-1650.

Phillips, J. M. 1995. Substrate Selection for Thin-Film Growth, MRS Bulletin, vol. 20, No. 4, pp. 35-39.

Piliarik, M. and Homola, J. 2009. Surface Plasmon Resonance (SPR) Sensors: Approaching Their Limits? Optics Express, vol. 17, No. 19, pp. 16505-16517.

Ramakrishna, S. A. 2009. *Physics and Applications of Negative Refractive Index Materials*, London: CRC Press.

Rayford II, C. E., Schatz, G. and Shuford, K. 2005. Optical Properties of Gold Nanospheres, Nanoscape, vol. 2, pp. 27-33.

Rich, R. L. and Myszka, D. G. 2004. Why You Should be Using More SPR Biosensor Technology, Drug Discovery Today: Technology, vol. 1, No. 3, pp. 3001-3008.

Rogers, P. H., Sirinakis, G. and Carpenter, M. A. 2008. Plasmonics Based Detection of NO_2 in a Harsh Environment, Journal of Physical Chemistry C, vol. 112, p. 8784-8790.

Rothschild, A. and Komen, Y. 2004. The Effect of Grain Size on the Sensitivity of Nanocrystalline Metal-oxide Gas Sensors, Journal of Applied Physics, vol. 95, p. 6374.

Rugar, D. and Hansma, P. 1990. Atomic Force Microscopy, Physics Today, vol. 43, pp. 23-30.

Saito, Y., Imamura, Y. and Kitahara, A. 2003. Optical Properties of YSZ Implanted with Ag Ions, Nuclear Instruments and Methods in Physics Research, Section B: Beam Interactions with Materials and Atoms, vol. 206, pp.272-276.

Saito, Y., Kumagai, H. and Suganamata, S. 1985. Coloration of Quartz by Metal-Ion Implantation, Japanese Journal of Applied Physics, vol. 24, p. 1115.

Saito, Y., Shang, D. Y., Kitsutaka, R. and Kitahara, A. 1997. Optical Properties of Cu-implanted $LiNbO_3$, Japanese Journal of Applied Physics, vol. 81, pp. 3621-3626.

Scaffardi, L. B. and Tocho, J. O. 2006. Size Dependence of Refractive Index of Gold Nanoparticles, Nanotechnology, vol. 17, pp. 1309-1315.

Schwartz, H. and Tourtellotte, H. A. 1969. The Journal of Vacuum Science and Technology, vol. 6, p. 373.

Sheth, A., Schmidt, H., and Lasrado, V. 1999. Review and Evaluation of Methods for Application of Epitaxial Buffer and Superconductor Layers, Applied Superconductivity, vol. 6**,** pp. 855-873.

Sirinakis, G., Siddique, R., Manning, I., Rogers, P. H. and Carpenter, M. A. 2006. Development and Characterization of Au-YSZ Surface Plasmon Resonance Based Sensing Materials: High Temperature Detection of CO_2, The Journal of Physical Chemistry B, vol. 110, p. 13508.

Smith, H. M. and Turner, A. F. 1965. Vacuum Deposited Thin Films Using a Ruby Laser, Applied Optics, vol. 4, No. 1, pp. 147-148.

Speight, J. G. 2005. *Lange's Handbook of Chemistry*, New York: McGraw Hill.

Tobiska, P., Hugon, O., Trouillet, A. and Gagnaire, H. 2001. An Integrated Optic Hydrogen Sensor Based on SPR on Palladium, Sensors and Actuators B, vol. 74, pp. 168-172.

Wagner, T. *Thin film Science*, Max-Plank-Institut fur Metallforschung, 70174 Stuttgart, Germany, from http://www.mpg.de/pdf/europeanWhiteBook/wb_materials_196_200.pdf

Xu, C., Tamaki, J., Miura, N. and Yamazoe, N. 1991. Grain Size Effects on Gas Sensitivity of Porous SnO_2-based Elements, Sensors and Actuators B, vol. 3**,** pp. 147–155.

Yamazoe, N. 2005. Toward Innovations of Gas Sensor Technology, Sensors and Actuators B, vol. 108**,** pp. 2–14.

Yoshioka, K., Tanihira, T., Shinnishi, K. and Kaneyasu, K. 2007. Development of Extremely Small Semiconductor Gas Sensor, Chemical Sensors, vol. 23, pp. 16-18.